ANALYSIS OF OPTICAL FIBER SPECKLE PATTERNS FOR DETECTION OF IVUS CATHETER TIP IN 3D SPACE: AN INTELLIGENT SENSOR RESEARCH

by

Soroush Razmyar

A dissertation submitted to the faculty of
The University of North Carolina at Charlotte
in partial fulfillment of the requirements
for the degree of Doctor of Philosophy in
Computing and Information Systems

Charlotte

2020

Approved by:

Dr. M. Taghi Mostafavi

Dr. Erik Saule

Dr. Mohammad R. Sayeh

Dr. Zachary Wartell

Dr. Mohamed-Ali Hasan

©2020
Soroush Razmyar
ALL RIGHTS RESERVED

ABSTRACT

SOROUSH RAZMYAR. Analysis of Optical Fiber Speckle Patterns for Detection of IVUS Catheter Tip in 3D Space: An Intelligent Sensor Research. (Under the direction of DR. M. TAGHI MOSTAFAVI)

This research study presents the architectural design and computational framework for an intelligent tracking sensor constructed from a multimode fiber optic. As laser light travels through an inhomogeneous medium, such as multimode fiber, the random interactions between light rays generate a circular output pattern commonly referred to as speckle patterns. Speckle patterns are highly responsive to the variation in the physical status of a multimode fiber. As a multimode fiber deforms, analysis of speckle pattern variations provides information about the external perturbations causing the deformation. This study presents a novel algorithm for calculating 3D transformations from a series of speckle patterns, which is modeled in three tiers.

In the first tier, we have performed a series of experiments to demonstrate, in a deforming multimode fiber, the structural variation of speckle patterns contains deterministic information. That also provides a systematic approach for measuring the deformation parameters of a multimode fiber using a convolutional neural network. Second, we have studied the oscillating behavior of multimode fiber as a function of its length to find the relationship between the sensor's heading direction and the deformation of its sensing fiber tip. By utilizing a Long Short-Term Memory model, we have demonstrated that long-term dependencies between the deformation parameters provide a stable and reliable indication of the intelligent sensor's direction. At the end, we have utilized these findings to develop a novel computational framework for the intelligent sensor. This computational framework includes a pipeline of deep learning models to extract features from a sequence of speckle patterns, and a motion model to estimate the trajectory of the sensor from the extracted features.

DEDICATION

No one was better at showing me how to be an everyday explorer than my Grandpa, when he bought a computer and made his "baboe3000" Yahoo ID at the age 86.

This work is dedicated to him.

ACKNOWLEDGEMENTS

First and foremost, I would like to thank my advisor Dr. M. Taghi Mostafavi who taught me so much and gave me unlimited support and help during my PhD journey. I learned a lot from his professional character and his insightful feedback.

I would also like to thank my dissertation committee members for their support and constructive feedback on this work. I was honored to have Dr. Erik Saule, Dr. Mohammad R. Sayeh, Dr. Zachary Wartell, and Dr. Mohamed-Ali Hasan in my committee. I would also like to thank Dr. Mohsen Dorodchi for offering his support towards my research. This work would have not been possible without the generous support of the Department of Computer Science and the Graduate Assistant Support Plan (GASP) award from the graduate school at UNC Charlotte.

I would like to express my deep appreciation and gratitude to my beloved wife, Samaneh Mahabadi for her continuous emotional support throughout this journey. Thank you for always encouraging me to pursue my passion.

Finally, I would like to thank my family for providing unlimited support during these years. Particularly my parents, Nasrin Tehrani and Rahmat Razmyar for providing me with the opportunity of exploring the world and always encouraging me to pursue higher education.

TABLE OF CONTENTS

LIST OF TABLES

LIST OF FIGURES

LIST OF ABBREVIATIONS

CNN Convolutional Neural Network

ECDF Empirical Cumulative Distribution Function

LSTM Long Short-Term Memory

MMF Multi-mode Fiber Optic Cable

PDF Probability Density Function

CHAPTER 1: INTRODUCTION

Major cardiovascular diseases have been the leading cause of death in the United States, accounting for over 614,000 deaths in 2015 and 761,000 in 2016 [1]. Coronary artery disease as the most common type of cardiovascular disorders accounts for one of six deaths in the United State [2]. Improvement in diagnostics of vascular plaques is one important factor that reduces these numbers. If these plaques could be detected at their early stages, proper treatment could be applied more effectively, which as a result may significantly increase positive clinical outcomes. This may be achieved by research and development of sensing technologies aimed to enhance the capabilities of currently available diagnostic systems.

Intravascular Ultrasound (IVUS) is a designated in vivo sensor to examine the internal structure of blood vessels. Since 1989, this catheter-based diagnostic tool has been used as the chief technology for visualization of the vascular lumen and arteriosclerotic plaque detection [3]. IVUS generates a series of two-dimensional cross-sectional (2D) images of the soft tissues within the artery, and thus, it provides physicians with a better opportunity to evaluate the type of plaque, the size of vessels, and the severity of the problem. Since the last decade, researchers have been investigating the possibility of transforming IVUS cross-sectional images into a 3D geometric reconstruction of blood vessels. Such transformation can be achieved through a three-step process. 1. extraction of the catheter 3D trajectory as well as the IVUS probe pose as it travels in vivo. 2. localization of the IVUS images along the extracted 3D trajectory. 3. updating the orientation of IVUS images according to the IVUS probe pose. While the later two steps are by no means simple, finding a proper method for extracting the 3D trajectory of IVUS probe in vivo has proven to be quite challenging. This is mainly due to the limitation of the IVUS system in providing the essential trajectory information.

During the past decade, researchers have investigated the fusion of IVUS and other imaging technologies, such as angiogram, to extract the trajectory of the catheter. Despite significant advances, the proposed approaches are known to have shortcomings that prevent them from being used safely, easily and effectively in everyday clinical practices [4]. The current systems are generally stationary, complex and require extended supervision in their operation. Moreover, many of them require a prolonged radiation exposure, which could be harmful to the patients [5, 6]. Also, they are costly, which limits their application on a broader scale. Medical instruments are not only preferred to be simple in operation but also expected to provide reliable data for physicians to facilitate the interpretation process.

One component that could advance the current state of this field is a dedicated position sensor for tracking the IVUS probe in vivo. This position sensor is desired to emit no harmful radiation and be compact enough for fusion to the IVUS systems. According to a recent review of cardiovascular 3D reconstruction techniques, such a sensor does not exist yet [7]. One possible approach, which has been considered in a few studies [8, 9], is utilizing optical fibers for extracting spatial information. Optical fibers have certain characteristics that make them an attractive technology for various in vivo or ex vivo procedures. They are disposable, relatively safe, and immune to electromagnetic fields. Additionally, multimode fibers are available with a wide variety of diameters and bending stiffness promoting adaptability. Moreover, it has already been demonstrated [8, 9, 10] that fusion of fiber optics with current biomedical instruments is a feasible approach.

This research focuses on devising a computational framework for a novel fiber specklegram tracking sensor so that it could estimate the motion trajectory of an object in 3D space. In particular, this work exploits the interferometry principles of a multimode fiber to estimate spatial transformation. The interference pattern of multimode fiber is referred as speckle pattern or specklegram, see Fig. 1.1. Speckle patterns are highly sensitive to deformation of a multimode fiber. Our approach is utilizing a pipeline of machine learning models to learn the relationship between a fiber optic deformation parameters and the structural variations of speckle patterns. We also provide a systematic approach for calculating 3D transformation of an object from speckle patterns variations.

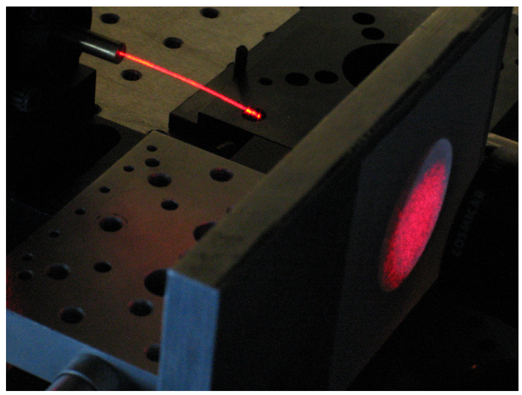

Figure 1.1: A speckle pattern is a projection of thousands of small clusters of lights emitted from a multimode fiber. An analysis of speckle patterns variations provides quantitative measurements of the physical status of the fiber.

The remainder of this document is organized as follows. In chapter 2 we review the proposed 3D vascular reconstruction techniques during the last 30 years. This chapter also covers fiber optic interferometry principle as related to this study. Chapter 3 explains the design and prototyping principles of the intelligent sensor in detail. This chapter also outlines the experimental setup, data collection process, as well as the validation procedure of the intelligent sensor. Chapter 4 and Chapter 5 provide a series of studies to illustrate the feasibility of utilizing speckle pattern analysis for position estimation. Chapter 6 provides a discussion on the performance of the intelligent sensor, and outlines the future steps of this research.

CHAPTER 2: BACKGROUND

The first section of this chapter provides a brief overview of the 3D vascular reconstruction techniques which have been proposed during the last 30 years. The literature suggests that 3D vascular reconstruction, even in an ideal laboratory setting, is challenging. The underlying difficulty is extracting the longitudinal shape of the vascular structure. Not only the proposed techniques are complex and time-consuming, but they also require prolonged exposure to harmful X-ray radiation. The fiber optic intelligent sensor explained in this work provides an alternative safer solution for tracking applications. To this end, the second part of this chapter provides a review of optical interferometry principles related to this study.

2.1 Vascular Reconstruction

Vascular reconstruction involves the process of collecting and analyzing medical imagery, typically in the form of series of gray scale images. The data collection hardware includes Intravascular Ultrasound (IVUS), Coronary Angiogram, Magnetic resonance imaging (MRI), Computerized axial tomography (CAT), Computed Tomography (CT), and Positron Emission Tomography (PET). The general approach for analyzing medical imagery is to extract interesting features by utilizing image processing pipelines for noise reduction, edge extraction, and segmentation. This pre-processing step is required because the data collection process is not done under ideal condition. The quality of the acquainted data is affected by a patient movements, the inherent sensing noise or imprecision of transducers, and visualization artifacts. Therefore, the current sensing hardware are required to be calibrated extensively to ensure optimum functionality. Among the mentioned imaging hardware, IVUS and X-ray coronary angiography are the most widely used technologies in clinical decision-making process [6, 11].

2.1.1 Intravascular Ultrasound Systems

When a patient need surgery to clean up blocked arteries, there is a lot of information doctors need before they can operate. One way to obtain such information is with the Intravascular Ultrasound (IVUS) technology that generates internal views of the blocked blood vessels. IVUS is a designated in vivo sensor for examine the internal structure of blood vessels. IVUS provides physicians with a better opportunity to evaluate the type of plaque that a patient has, the size of vessels, and the severity of the problem by showing a 360° view of internal structure of the veins, as shown in Fig. 2.1 [12].

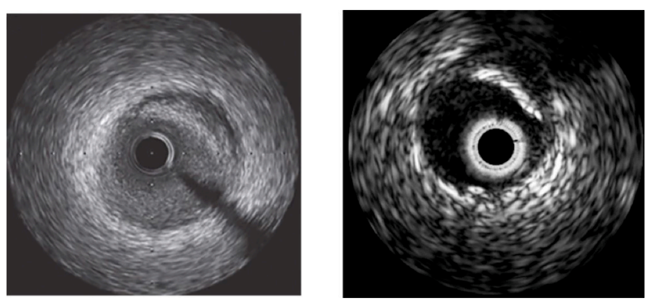

Figure 2.1: Examples of IVUS echo-graphic 2D images showing a 360° view of a blood vessel.

IVUS imaging operation involves the following steps [13, 14]:

1. Converting the electrical pulse into high-frequency sound waves (ultrasounds).

2. Emitting and capturing the sound waves as reflected by tissues.

3. Converting back the reflected ultrasounds into electrical signals.

4. Visualizing the electrical signals.

In clinical application a guide wire is inserted into the vessel. Then, doctors inserts and advances the catheter over the guiding wire inside the patient's body and into the artery. The imaging process starts during the pullback phase of operation. The speed of an IVUS pullback is about 0.5 – 1.0 mm per second. By constantly receiving the reflection of the sound waves, IVUS systems are capable of generating images at the rate of 25-30 frames per seconds [15]. The spatial resolution of IVUS systems is about 80-100 μm. The most important limitation of IVUS for 3D reconstruction of blood vessels is inability to provide the longitudinal shape of the blood vessels. Fig. 2.2 illustrates a simplified diagram of IVUS pullback acquisition.

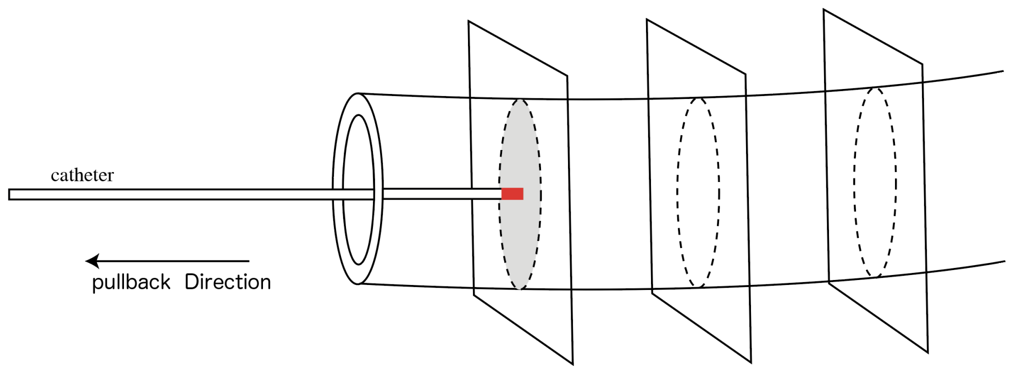

Figure 2.2: IVUS captures a series of cross-sectional images during the pullback phase. The longitudinal shape of the blood vessels can not be extracted directly from the IVUS images. Another technology, such as angiography, will be required to track and extract the trajectory of IVUS catheter.

2.1.2 IVUS 3D Volume Reconstruction Techniques

Since the early days of the IVUS technology, researchers have investigated the possibilities of reconstructing a vessel 3D geometry through the utilization of a series of 2D images. Due to the limitation of IVUS in providing the shape of vessels, another imaging modality, such as angiography, is required to provide such information. Coronary angiography provide an X-ray visualization of the heart's chambers and the surrounding blood vessels. This procedure is often performed to identify any narrowed or clogged areas of coronary arteries that prevents blood from reaching to heart muscles. Similar to the IVUS, angiography is an invasive procedure, which requires a catheter to be inserted and tracked into the blood vessels. Angiography catheters are flexible plastic tubes, which are used to inject X-ray dye inside the vessels. Due to the provided contrast by the injected dye, the fluoroscope captures X-ray images, or angiograms. The fluoroscope equipment includes an X-ray source and an intensifier which, are installed on two opposite sides of a C-shaped arm. This C-arm rotates in two directions around an imaginary central point called the iso-center, see Fig. 2.3 [16]. It also moves in three directions. Thus, the angiography equipment has five degrees of freedom.

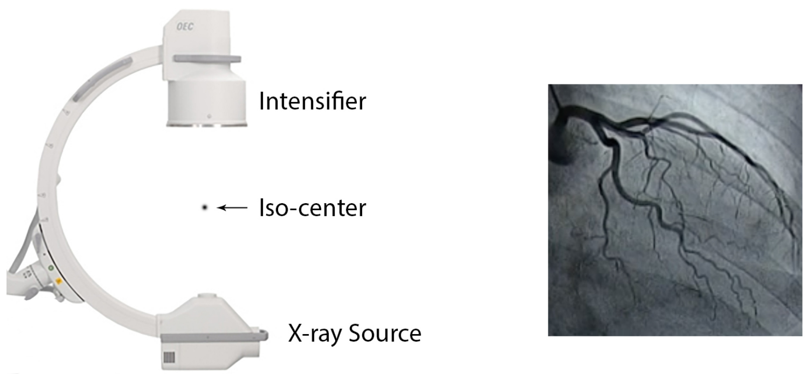

Figure 2.3: (Left) Example of angiography C-arm. A patient is positioned at the 'iso-center' location. Through X-ray imaging this system provides 2D visualization of the blood vessels, as shown in the right panel. Angiography process requires prolonged exposure to harmful X-ray radiation.

During the late 80s and early 90s, a trend of studies focused on reconstruction of blood vessels by using images taken during angiography. In 1986, Wollschlager et al. [17] introduced a mathematical model that described the characteristics of a standard two X-ray biplane angiography system. Throughout the literature, their model is referenced as the "classic iso-centeric geometry model", because it assumed only one fixed iso-center for both X-ray systems. In 1991, a paper by Wahle et al. [18] presented the first 3D visualization method, which was implemented based on the classic iso-centeric geometry mode. In that work, the authors used the fixed iso-center point of the two X-rays as a reference point. However, it became clear that the assumption of a fixed iso-centeric point was not realistic. In practical applications, the movement or rotation of the instruments alters the iso-centeric point. Due to this shift, the iso-center reference point became blurry or undetectable. In a sequential paper [19], the authors improved the classic iso-centeric geometry model to account for a variable iso-center reference point. Moreover, they presented several algorithms to correct the model based on the effect of the missing points [20]. Despite promising a positive outlook and providing an overall visual reconstruction of coronary vessels, these approaches were not capable of providing any information on the internal structure of veins or plaques. Considering the available technology of the time, it was the fusion of biplane angiography and IVUS that made the realistic reconstruction of blood vessels possible. Fig. 2.4 illustrates an example of vascular reconstruction process according to the IVUS X-ray coronary angiography approach, in a laboratory setting. X-ray images are stereoscopically analyzed to extract the location of the catheter tips.

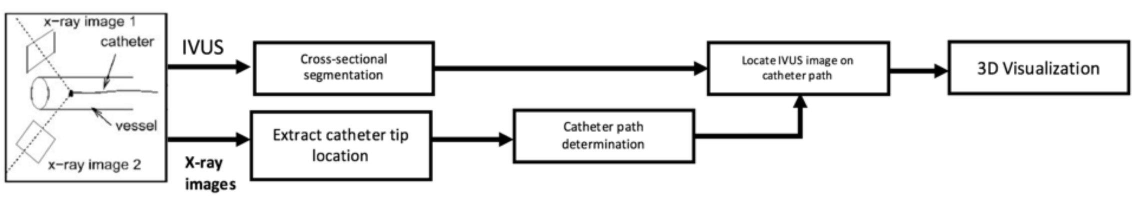

Figure 2.4: IVUS X-ray based vascular reconstruction pipeline.

Some of the early studies on 3D reconstruction treated the vessels as straight lines [21, 22, 23, 24]. Here, the idea was to construct a 3D cylinder resembling the vessel volume. Series of IVUS 2D images were taken at predefined intervals; and placed along a straight line resembling the catheter path. This approach was a breakthrough technology, still it suffered from one major limitation: its inability to provide the actual shape of the vessels. To address this obstacle, various technologies were proposed to obtain spatial information from the biplane angiography. Laban et al. [25] developed the ANGUS method, which combined biplane angiography with images obtained from IVUS. Their model was a break breakthrough approach since it provided a realistic catheter path. The major limitation of ANGUS was the assumption that the catheter's longitudinal centerline represents the curvature of vessels [26]. Also, their work did not consider the catheter's change of orientation during the pullback process. In another study, Evans et al. [27] attempted to acquire the IVUS images and their coordinates simultaneously. Also, a transformation matrix was used to find the 3D positions of the IVUS coordinates from two biplane views. Their design decreased the overall reconstruction process. Similar to the previous studies, it did not address the orientation of the catheter tip.

Another study by Prause et al. [28] introduced a robust algorithm for tracking the orientation of the catheter based on the previously traversed 3D trajectory. During the pullback process, the catheter changes its trajectory plane in respect to the world reference system. As the catheter's orientation changes in the world frame, its new local orientation were updated based on the previous local ordination. Their solution successfully measured the orientation of the catheter by about 1% per cm overestimation.

The approach of Subramanian et al. [29] to the 3D vascular reconstruction was to manually selecting a few key point from X-ray images for an accurate visualization of the arterial vessels. A few X-ray images were utilized for ext rating the catheter tip's location at key points along the vessel length. Then, the catheter's trajectory was estimated by interpolation of a spline according to the Kochanek-Bartels mathematical model [30]. They also used a motorized pullback IVUS system to reduce the catheter's twists. All IVUS images were oriented based on a known reference direction. Once the locations of all images were cleared, the 3D volume was created by combining the intensity of IVUS images at all lattice points. Through this novel approach, a more realistic 3D volume was constructed. Another key advantage of this work was the reduction in the number of required angiograms, which promoted safety. In comparison, this approach was time-consuming, which affects its usability for real-time applications. Bourantas et al. [31] introduced a new algorithm to extract the catheter path from angiograms with higher accuracy. Their approach was capable of providing a complete path from images with missing or unclear segments. Next, Zheng [32] improved the accuracy of volume construction by addressing issues such as axial position, spatial orientation and surface fitting. Finally, Carlier et al. [33] proposed a real-time fusion of IVUS or OCT with angiograms through which automated or semi-automated image processing techniques are used to extract the 3D path.

A review of recent progress on 3D reconstruction of coronary arteries [6] suggests that tracking the catheter's trajectory, even in a contorted laboratory setting, is challenging. Analyzing X-ray images is a workable solution for extraction of the catheter path, but far from an ideal solution. First and foremost it requires a prolonged exposure to X-rays radiation, which is harmful to humans. Image noise, low contrast and even overlapping blood vessels affects the accuracy of the path extraction techniques. Also, due to their dependency on some degree of human intervention, none of the proposed techniques could be performed in real-time. Moreover, the reconstructed curvature according to this approach suffers from accumulated error. Finally, the assumption that catheter will follow the vessels' centerline was not quite realistic. While utilizing a motorized IVUS transducer reduces the undesired catheter change of location or orientation, it does not eliminating it. Several factors can cause the catheter to shift significantly from the vessels' centerline. These factors include the vessels' curvature shape or diameter, and movement resulted from heartbeat or breathing. While the current modalities are promising, they still need further refinements.

A position sensor constructed from a fiber optic cable has the potential to provide an alternative solution for those challenges. This leads to the reduction of the diagnosis-treatment procedure. Fiber optics are flexible, lightweight and small in diameter. Therefore, they are a natural fit for invasive medical applications.

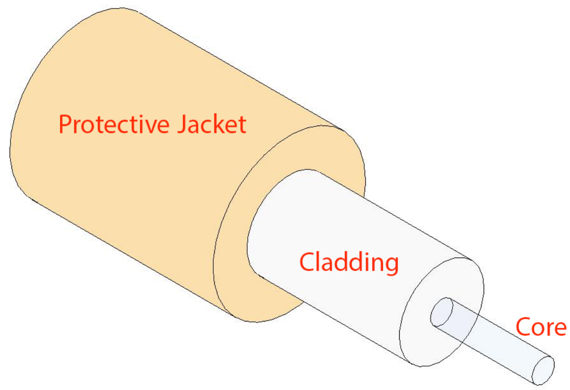

Figure 2.5: The structure of a typical fiber optic cable. Light propagates in an optical fiber because the index of reflections of the core and the cladding layer are different.

2.2 Fiber Optics

Optical fibers are thin ($8\mu m$ *to* $1000\mu m$) and flexible optical waveguides, which are commonly used for long distance light transmission in telecommunication applications. A typical fiber optic cable has three layers: core, cladding, and a protective jacket, shown in Fig. 2.5. The core, or the central part of the fiber, is the area through which the light signals travel. The cladding surrounds the inner core layer. While both core and cladding layers are composed primarily of silica glass, the core is denser and has a higher index of reflection than the cladding. The difference between the index of reflection of the core and the cladding layer allows the light waves to travel in a series of zig-zag bounces inside the fiber.

There are two classes of fiber optics: single-mode and multimode. Whether a fiber is multimode or single-mode depends on its core diameter, core/cladding reflective indices and the wavelength of the light. Single mode fibers have smaller cores (8–$10\mu m$), which allows only one mode of light to pass through. Also, they have low attenuation, which makes them suitable for long distance communications. For a particular wavelength λ, the maximum core diameter D in which light can be transmitted in a single-mode is:

$$D < \frac{2.405\lambda}{\pi\sqrt{n_{co}^2 - n_{cl}^2}} \tag{2.1}$$

Where n_{co} and n_{cl} are refractive indexes of the core and cladding [34, 35]. If the core diameter is any larger than D, the fiber operates in multimode regime. multimode fibers have larger core diameters ($20 - 1000\mu m$), which allow multiple pathways of light to propagate simultaneously. In comparison to single-mode fibers, multimode fibers have higher attenuation rate. Therefore, are mostly used for short distance data communication (i.e. LAN).

Although optical fibers are mainly used for data transmission, they have characteristics that make them a suitable technology for sensing applications. They are flexibility and light weight, inexpensive and available, so they can be easily replaced. Moreover, their exceptional thinness along with their ability to operate independently from any source of electrical power makes them a suitable candidate for various industrial or medical applications. In this respect, during the past decades, numerous studies have been devoted to producing a range of fiber-based sensing principles which can be applied to variety of sensing applications. Comprehensive reviews of key development in fiber sensing technology are presented in these articles [36, 37]. The sections that follow reviews the characteristics of two types of fiber sensors that is more relevant to this research. Please note in this dissertation, optical fiber, fiber optic cable, and fiber will be used interchangeably.

2.2.1 Fiber Bragg Gratings (FBG)

Gratings are invisible and permanent periodic reflectors, created in segments of a single-mode fiber. When an incidence spectrum of light propagates through the gratings, a specific wavelength, i.e. Bragg wavelength, is reflected back while the rest of the spectrum is transmitted unaffected. The Bragg wavelength λ_B depends on the refractive index of the grating in the fiber core n and the grating period Λ [38]:

$$\lambda_B = 2n\Lambda \tag{2.2}$$

During the past decade, this relationship has been utilized for development of FBG-based sensors. From a physical point of view, strain is a macroscopic measure of structural deformation [39]. As a fiber optic deforms, strain ϵ is applied the fiber gratings, which consequently, shifts the reflected wavelengths $\Delta\Lambda_B$ from its initial value Λ_B. The relative shift in the Bragg wavelength $\Delta\lambda_B/\lambda_B$ can be estimated by:

$$[\frac{\Delta\lambda_B}{\lambda_B}] = C_S\Delta\epsilon + C_T\Delta T \tag{2.3}$$

where C_S and C_T are constant values representing the coefficient of stain and coefficient of the temperature, respectively. By monitoring the temperature fluctuation, or with the assumption of $\Delta T = 0$, the change in strain value $\Delta\epsilon$ can be measured dynamically [40, 41]. Researchers have used this principle to propose various strain and temperature measuring systems. In addition, application of FBG sensors has been extended to measure other physical quantities such as acceleration, pressure, displacement. While these FBG-based modalities are similar the other types of fiber sensors in terms of compactness and flexibility, they are more sensitive and accurate.

Additionally, a unique advantage of the FBG technology is that it allows measurement points to be fabricated as an array of independent sensors along the same fiber, enabling distributed sensing. This is an interesting feature in the context of the vascular reconstruction since a trend of studies have focused on FBG-based shape sensors [42, 40, 43]. In theory, fusion of a fiber shape sensing sensor and IVUS seems like a workable solution for extracting the catheter path [8, 9, 10]. Yet, there are several issues that are left to be solved. FBG sensor measurements are highly sensitive to variation in temperature. It has been shown that when used in vivo, a shape sensor may go through a change of temperature up to 10° C [44]. Failing to consider this change of temperature during the modeling process may significantly reduce the accuracy of the reconstructed curves.

Additionally, the current generation of shape sensors operate by measuring the reflected light from multiple FBG structures. The loss of reflected light in the fiber and resolution of the interrogator are another sources of error that decreases the accuracy of FBG sensors. Fabrication challenges are another source of error that influence the accuracy of such sensors [43, 45]. These challenges include: proper arrangement of the FGB sensors, accurate cross-sectional angular alignment of FBGs, and precise installment of multiple fibers in equal distances from the center of the structure. Due to the small size of fibers, high-tech manufacturing techniques are needed to overcome the fabrication issues. Therefore, the FBG sensors and the interrogator apparatus are complex and more expensive in comparison to the other fiber-based sensors [38]. Though this research study focuses on specklegram-based sensing instead of FBG-based approach, we provided this brief overview to emphasize the importance and potential of FBG sensors for medical applications. This area of research is relatively new and further improvement will be required before FBG sensors could effectively be used in the clinical settings. A more comprehensive literature review of FBG sensors can be found in [46].

2.2.2 Specklegram Sensors

As laser light travels through an inhomogeneous medium such as a multimode fiber the random interference between light modes generates a circular output pattern commonly referred to as speckle patterns (or specklegram) [34], see Fig. 2.6. Although a comprehensive mathematical model for decoding the specklegram interference has not being developed yet [47], some characteristics of speckle structure are as follows. In a multimode step-index fiber the number of speckles and the number of modes are

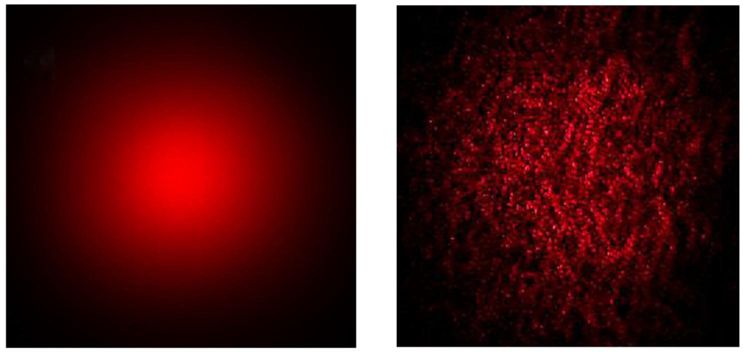

Figure 2.6: (left) Gaussian beam profile of a single-mode fiber is produced by only one light mode. (Right) Beam profile of a multimode fiber, i.e speckle pattern, is generated due to the interaction of several light modes.

approximately equal [34]. The number of individual speckles is expressed by:

$$V \approx \frac{2\pi d_{co}}{\lambda_\circ}(NA) \tag{2.4}$$

$$NA = \sqrt{n_{co}^2 - n_{cl}^2} \tag{2.5}$$

where V is the number of modes, $\lambda_\circ$ is the wavelength of light in the air, NA is the numerical aperture of the fiber, d_{co} is the fiber diameter, and n_{cl} and n_{co} are refractive indexes of the cladding and the core [34, 47]. When $V < 2.405$ fiber exhibits single-mode behavior. [35]. According to the equation 2.4, the number of individual speckles increases for multimode fibers with a larger core diameter and higher NA. Similarly, increasing the wavelength of the laser light reduced the number of speckles.

Fiber specklegram sensors (FSS) are type of measuring devices that utilize interferometry principles to retrieve information about the physical status of a fiber. As illustrated in Fig. 1.1, a typical FSS configuration includes a multimode fiber that is powered by a coherent light source (laser), a diffuse surface to visualize the speckle patterns, and an image acquisition device to record the pattern. The FSS operation principle is as follows: assuming I_i denotes the intensity of each individual speckle, then the overall intensity of specklegrams I_{total} is approximately constant:

$$I_{total} = \sum_{i=1}^{V} I_i = constant, \tag{2.6}$$

where V is the total number of speckles [48]. As light enters from one side and propagates through the fiber cable, fiber deformation due to the presence of external forces, alters the the intensity distribution of speckle pattern at the other side: some become brighter and some dimmer. A CCD camera records speckle variation over time. An analysis of the variation in intensity of speckle pattern provides information about those external perturbation. This phenomenon has been widely used to measure physical phenomena such as temperature [49], displacement [50], vibration [48, 51, 52], and force measurement [53]. More recently, speckle pattern sensing is utilized for tactile arrays for human-robot interaction [54].

The main advantages of using the fiber optic specklegram sensors – in comparison to conventional sensors – include compactness, low cost, and adaptability. However, there are complications that limit their application. Generally speaking, specklegram sensing is achieved by analyzing, or utilizing intensity variation of speckle patterns in time. Theoretically [55], despite the fact that the intensity of individual speckle dots varies in response to external stimuli, the overall intensity of specklegrams is assumed to be constant. In practice, that is not the case. The measurement error due to the light source fluctuation is common to speckle-based sensors [56]. Thus, a continuous referencing mechanism is needed to monitor the light source and calibrate the sensor to reduce the effect of the light source power fluctuation. In other words, without a referencing mechanism, which often tends to be complex, the measurement will suffer from additional random noise. Contrarily, using a reference mechanism is far from an ideal solution as it decreases the dynamic range of such sensors while making implementation more complex.

To address some of these concerns, some studies have devised computer vision techniques to analyse speckle patterns. One attractive approach is to compare a sequence of speckle images captured during a time interval using various template matching algorithms. Template matching methods relies on segmentation of an image in to region of interest, and quantifying the degree of similarity of each region to a reference template applying a correlation function. Since the reference image is usually the first captured image during each interval, template matching is an attempt to eliminate the need for a continuous referencing mechanism. In this sense, the challenge shifts to defining a correlation function robust to intensity fluctuation. The common correlation functions, which have been studied extensively are Zero Mean Normalized Cross-Correlation (ZNCC) [57], Phase-Only Correlation (POC) [58], Sum of Squared Differences (SSD) [59], and Ratio Image Uniformity (RIU) [59].

While image matching techniques have provided a significant improvement in the specklegram-based sensing, they are not without limitations. A recent study by Fujiwara et al. [60] evaluated several image matching algorithms for specklegram sensing. According to their results, all common image matching methods provided equivalent stable performance. However, the dynamic range of the ZNCC method shown to be limited since it saturates to a minimum value when an speckle image becomes substantially different from the reference frame [60, 61]. Also, POC, SSD and RIU were highly sensitive to intensity variations which, limits their applications in detection of subtle deformations. These results suggests while image matching techniques provide a relatively simple sensing alternative, their practical applications are not trivial and might be challenging.

Another drawback common to many of the speckle-based sensors is is the limitation of their functionality to one axis of freedom [49, 62, 63, 53]. This limitation may be of considerable importance since many physical phenomena, such as force or displacement have a vector nature: they have a magnitude as well as a direction. Recently published reviews of specklegram-based sensing literature suggest that most techniques gravitate toward magnitude estimation of acting stimuli [64, 60]. Indeed, only a few studies have been focused on the estimation of the direction of deformation or retrieving spatial information using speckle patterns [65, 66]. Although promising results of these studies are limited due to the overall size of such systems, accuracy or stability.

With advancement in computing technology, neural network models have been utilized in the speckle sensing applications for a variety of purposes including stress measurement [67], pH. Measurement [68], and structural health monitoring [69]. The possibility of using neural network was further explored to construct an intelligent shape sensor [65]. Other application of neural network in specklegram based sensing included modalities for force measurement [63], distributed acoustic sensing [70], and a spatially-resolved sensing system [71]. These reports suggest that a neural network based fiber optic sensors may provide a more reliable analytical alternative compared to the conventional sensors, which applications are limited due to their physical characteristic, accuracy or performance.

CHAPTER 3: METHODOLOGY

This research is toward the “intelligent” aspect of the sensor: a computational framework to estimate spatial transformation by analyzing raw inputs. In this chapter we explain the architecture design, motion model and validation process of an intelligent sensor to track motion. The presented sensor incorporates a multimode fiber optic as a transducer. We also utilize a pendulum system to construct a comprehensive dataset for speckle pattern analysis. Please note in this study, ’the intelligent sensor’ and ’the sensor’ will be used interchangeably.

3.1 Fiber Optic Intelligent Sensor

Fig. 3.1 presents the architecture design of the intelligent sensor. The sensing transducer consists of an elastic multimode fiber mounted on a rigid base. One end of the multimode fiber is coupled to a laser module and the other open end is free to move toward a diffuse surface. In such configuration, the “sensing” mechanism of the sensor is as follows. Ideally, this sensor will be co-located with the IVUS catheter over a guide wire , and follows its motion. During the pullback phase, an axial force is applied to the transducer and pulls it back. In reaction to this force, the elastic fiber deforms and its tip deviates from the resting position. This deformation changes the speckle patterns. Analyzing these variations provides “directional hints” to describe motion of the system. In the laboratory setup, speckle patterns are projected onto a diffused surface and captured with a high frame rate camera, which is mounted in parallel to the diffuse surface. Although this configuration it does not suit the “in vivo” applications, it provides a mean of testing our approach. Fig. 3.2 illustrates an alternative architecture for in vivo applications. While work is toward a clinical

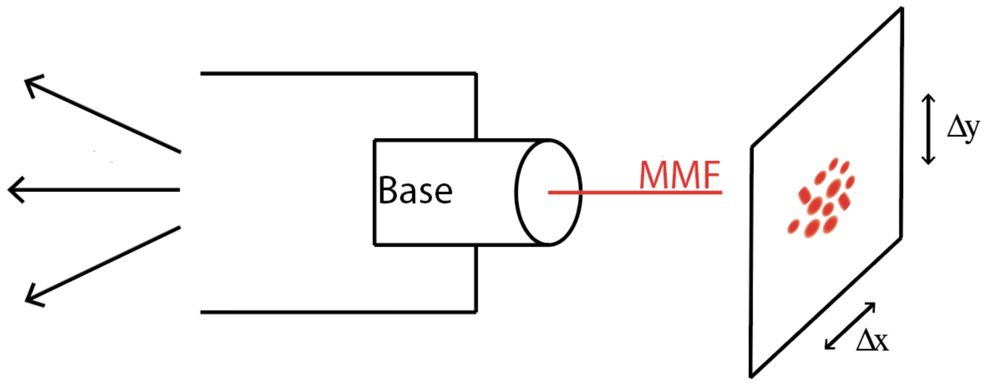

(a) Schematic design of the intelligent sensor.

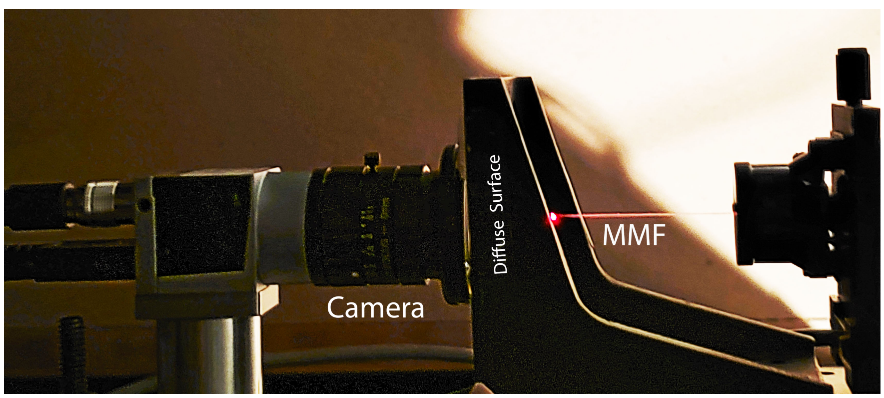

(b) Laboratory configuration of the sensing transducer.

Figure 3.1: (a) The architecture design of the intelligent sensor includes a rigid base and an elastic multimode fiber (MMF). The speckle patterns are projected on a diffuse surface, and captured by an image acquisition device. As the sensor travels in space, the tip of the MMF deviates from its resting position. Consequently, the speckle patterns change. Displacement in two axes of movement are estimated through analysis of speckle patterns. (b) The laboratory implementation of the sensing transducer, in which a high frame-rate camera captures 115 speckle patterns per second from a diffuse surface.

application, the hardware manufacturing details of the in vivo setup are beyond the focus of this research.

Figure 3.2: An example of an in vivo setup. This setup is consisted of a multimode fiber (MMF) and a mirror (M) attached to the end of the fiber. Lights enters into the MMF and is reflected by the mirror. The resulting specklegrams are recorded by a detector at the other side of the fiber.

3.1.1 Motion Model of The Intelligent Sensor

Generally speaking, there are two classes of motion models: kinematic models which, describe the motion of an object without considering the acting forces, and dynamic models that attempt to embody the relationship between forces and motion. In other words, kinematic models are simplified dynamic models where mass and external forces such as gravity are ignored. Due to this simplification, while kinematic models are more tractable, they are less accurate than dynamic models. Despite this, the kinematic models are capable of approximating a system's the actual dynamics when the acceleration is not significant, i.e. constant speed. As we will demonstrate in the work, kinematic models are sufficient enough to describe the motion of our position sensor.

The in vivo nature of this research allows the following relaxation to be made regarding the motion of the intelligent sensor. 1) The system is fully calibrated, meaning the location and orientation of the camera in respect to the fiber optic does not change. 2) The motion of the fiber's tip is restricted to a plane perpendicular to its central axis. 3) Most IVUS equipment provide means of controlling the motion

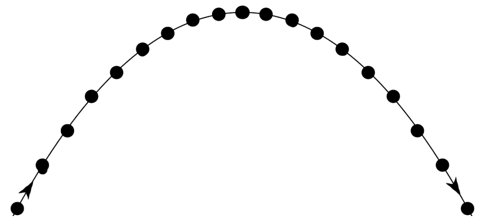

Figure 3.3: Using a high sampling rate, the traversed path of the intelligent sensor can be represented by a sequence of trajectories with constant curvature. The overall trajectory is shown in 2D but generalizes to 3D.

of the catheter during the procedure. Thus, we assume the displacement of the sensor along its central axis is a known parameter. 4) Since the sampling rate of the intelligent sensor is in the order of milliseconds $\geq 115fps$, the traversed path of the sensor between each sampling moment is assumed to be a continues curve of constant curvature, see Fig. 3.3. 5) Finally, the coordinate system of the camera is assumed to be the same as the coordinate frame of the intelligent sensor.

These assumptions provide a foundation on which to develop the motion model of the intelligent sensor. As the sensor travels through space, the camera captures images at discrete time instances. Let $I_{0:k} = \{I_0, ..., I_{k-1}, I_k\}$ represents the collection of all captured speckle images, and I_k be speckle images captured during the time frame k. The sensor's transformations between t_k and t_{k-1} are related by a 4×4 matrix $P_{k,k-1}$ with the following structure:

$$P_{k,k-1} = \begin{pmatrix} R_{k,k-1} & T_{k,k-1} \\ 0 & 1 \end{pmatrix} \tag{3.1}$$

where $R_{k,k-1}$ is a 3×3 direction cosine matrix (DCM), $T_{k,k-1}$ is a 3×1 translation vector, and $0 < n < k$. Next, let $P_{0:k} = \{P_{1,0}, ..., P_{k,k-1}\}$ represent the overall motion of the sensor during interval 0 to k. Also, assume $W_{0:k} = \{W_{1,0}, ..., W_{k,k-1}\}$ denote the motion of the sensor in the world coordinate system (WCS), where W_0 being the sensor's initial position at time $t = 0$, equal to I or any arbitrarily value. Then, the

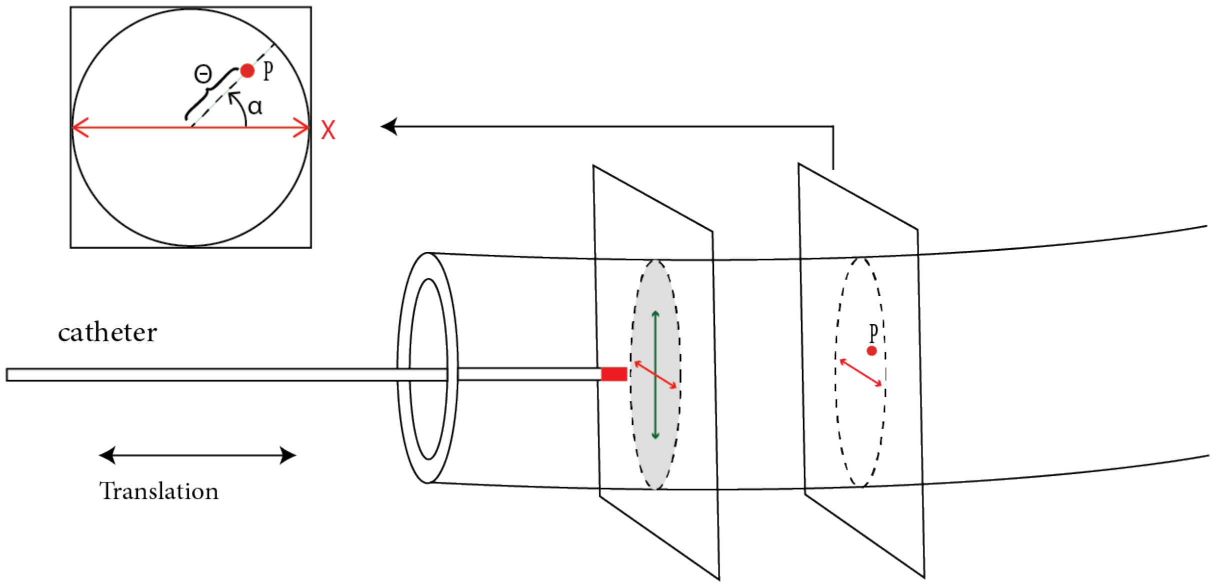

Figure 3.4: The motion of tip of catheter has three degrees of freedom: translation along the length of the catheter, and a deformation in a plane perpendicular to the axis of translation. Using a polar coordinate, the deformation magnitude and the direction of bending of the tip of the catheter are represented by its distance from the origin $\theta \geq 0$, and its angle with the polar axis $\alpha \in [0, 2\pi]$, respectively.

current W_k can be calculated by combining all transformation $P_{0:k}$ using:

$$W_k = W_{k-1}.P_k \tag{3.2}$$

Here, our goal is to measure the relative transformation P_k using a sequence of speckle images I_k, and to combine them according to the equation 3.2 to recover the overall trajectory $W_{0:k}$ of the intelligent sensor. Consider a hypothetical scenario in which a fusion of IVUS and the intelligent sensor has been inserted over a guide-wire into a constrained environment, i.e: blood vessel, see Fig. 3.4. This system has three degrees of freedom (DOF): two bending directions in the tip location (2DOF) as well as a translation(1 DOF). Since the motion of the sensors is controlled by the IVUS cable, the overall system can be modeled as a cable-driven continuum structure. This approach has been explored in numerous studies such as [72, 73, 74, 75]. Therefore, we employ the same geometry-based approach to model the motion of the sensor.

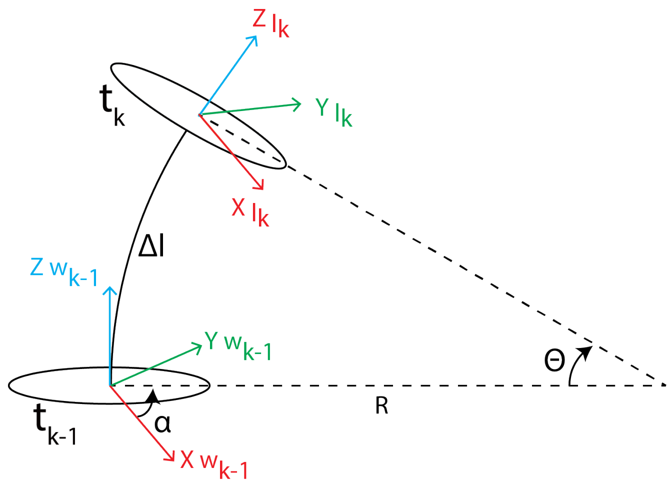

Figure 3.5: Geometrical illustration of the translation of the intelligent sensor during the time interval $t_{k-1} \to t_k$. The current state of the sensor at time t_K can be calculated by updating its previous state at the time t_{k-1} according to the α, θ *and* Δl parameters.

Consider Fig. 3.5, which represents the displacement of the intelligent sensor during the time frames $t_{k-1} \to t_k$ using the following parameters:

- $\{X_{w_{k-1}}, Y_{w_{k-1}}, Z_{w_{k-1}}\}$ sensor's state at time t_{k-1} in WCS.
- $\{X_{l_k}, Y_{l_k}, Z_{l_k}\}$: sensor's local (LCS) state at time k in .
- Δl sensor's displacement along its central axis during $t_{k-1} \to t_k$
- $\theta \geq 0t$ is the heading direction of the sensor during $t_{k-1} \to t_k$
- $\alpha \in [0, 2\pi]$ represents the direction of bending during $t_{k-1} \to t_k$
- R radius of the path curvature.

With the assumption of constant curvature ($R = \frac{\Delta l}{\theta}$), the process of updating the sensor's transformation during the time interval $t_{k-1} \to t_k$ are:

1. $T_{k,k-1}$: Translation the of the WCS_{k-1} to LCS_n.
2. $R_{Z,\alpha}$: Rotation of LCS_k around Z-axis for α.

3. $R_{Y,\theta}$: Rotation of LCS_k around y-axis for θ.

4. $R_{Z,-\alpha}$: Rotation of LCS_L around Z-axis for $-\alpha$.

These transformation are formulate as:

$$W_{k-1}.P_k = \begin{pmatrix} R_{Z,\alpha} & 0 \\ 0 & 1 \end{pmatrix} \begin{pmatrix} R_{Y,\theta} & T_{k,k-1} \\ 0 & 1 \end{pmatrix} \begin{pmatrix} R_{Z,-\alpha} & 0 \\ 0 & 1 \end{pmatrix} \tag{3.3}$$

According to the geometry principles, the transformation $T_{k,k-1}$ can be measured from:

$$T_{k,k-1} = \frac{\Delta l}{\theta} \begin{pmatrix} C\alpha(1 - C\theta) & S\alpha(1 - C\theta) & S\theta \end{pmatrix} \tag{3.4}$$

and the rotation matrix $R_{k,k-1}$ is [72, 73, 74, 75]:

$$R_{k,k-1} = \begin{pmatrix} R_{Z,\alpha} & 0 \\ 0 & 1 \end{pmatrix} \begin{pmatrix} R_{Y,\theta} & 0 \\ 0 & 1 \end{pmatrix} \begin{pmatrix} R_{Z,-\alpha} & 0 \\ 0 & 1 \end{pmatrix} =$$
$$\begin{pmatrix} C^2\alpha C\theta + S^2\alpha & C\alpha S\alpha C\theta - C\alpha S\alpha & C\alpha S\theta \\ C\alpha S\alpha C\theta - C\alpha S\alpha & S^2\alpha C\theta + C^2\alpha & S\alpha S\theta \\ -C\alpha S\theta & -S\alpha S\theta & C\theta \end{pmatrix} \tag{3.5}$$

where, $C\alpha = \cos\alpha$, $C\theta = \cos\theta$, $S\alpha = \sin\alpha$, and $S\theta = \sin\theta$. Through an iterative calculation, the current position of the sensor is calculated by applying the equations 3.5 and 3.4 into 3.2. Note that Δl is a known parameter, and therefore, the problem of motion estimation comes down to measuring the θ and α angles using a sequence of speckle images I_k.

3.1.2 Methods of Sensor Evaluation

The intelligent sensor must be validated to ensure that it performs as expected. In order to validate the sensor, a separate tracking sensor will be required to provide the reference measurements, i.e. ground truth values. When traveling a control path, the reference sensor and the intelligent sensor produce two sets of estimations at some sampling rate. These estimations represents two trajectories, or two distributions. Ideally, the measurements of the intelligent sensor will have a similar distribution to the reference sensor's measurements. The statistical procedure to evaluate the measurements of the intelligent sensor is as follows:

1. Constructing the reference distribution: the central limit theorem states the mean of a sufficiently large sample set is proximately equal to the population mean. To apply this theorem, several observations of the reference sensor traveling a control path will be collected. Each observation will be defined by a pair of two sets of consecutive measurements such as M_{ref} and M'_{ref} taken from the reference sensor:

$$M_{ref} = \{(x, y, z)_i\} : i \in \{1..p\} \tag{3.6}$$

$$M'_{ref} = \{(x', y', z')_i\} : i \in \{1..p\} \tag{3.7}$$

where i is the sampling order and p denotes the number of samples within each set. For each observation, the absolute difference of sampled points in 3D space will be calculated by examining the planar projections. Let d_c be the absolute difference of the sampling points for every observation. Then, the difference between pairs of sampling point produces a set P such as:

$$P : \{d_c = \sqrt{(x_i - x'_i)^2 + (y_i - y'_i)^2 + (z_i - z'_i)^2} : i \in \{1..p\} \tag{3.8}$$

$$\overline{d}_{obs} = \frac{1}{p}\sum_{c=1}^{p} d_c \tag{3.9}$$

where $\overline{d}_{obs}$ is the mean distance of reference sensor's measurements as it travels the control path in one observation. The central limit theorem states when observations are repeated many times, the computed values of the average follows a normal distribution. Therefore, after collecting k observations, the reference distribution have the mean $\overline{d}_{ref}$ and variance σ_{ref}:

$$\overline{d}_{ref} = \frac{1}{k}\sum_{n=1}^{k}\overline{d}_{obs_n} \tag{3.10}$$

$$\sigma_{ref} = \sqrt{\frac{1}{k}\sum_{n=1}^{k}(\overline{d}_{obs_n} - \overline{d}_{ref})^2} \tag{3.11}$$

2. Constructing the intelligent sensor's distribution: the intelligent sensor's distribution will be obtained through the same process as the previous experiment. Here, each observation is defined by a pairs of two sets of consecutive measurements such as M_{ref} and M_{new} taken from the reference sensor and the intelligent sensor:

$$M_{ref} = \{(x, y, z)_i\} : i \in \{1..p\} \tag{3.12}$$

$$M_{new} = \{(x^{'}, y^{'}, z^{'})_i\} : i \in \{1..p\} \tag{3.13}$$

and

$$P : \{d_c^{'} = \sqrt{(x_i - x_i^{'})^2 + (y_i - y_i^{'})^2 + (z_i - z_i^{'})^2} : i \in \{1..p\} \tag{3.14}$$

then, following similar steps as the experiment 1, the sample distribution of the mean differences between the intelligent sensor and the reference sensor is constructed. This sample distribution will be called the intelligent sensor distance distribution, or in short, the intelligent sensor distribution.

3. Let k and l represents the number of observation that were used to construct the reference and the intelligent sensor distributions, respectively. Assuming $k \ggg l \ggg 1$, t-test can be used to test whether the intelligent distribution is significantly different from the reference distribution. Let μ_{ref} represent the mean for the reference distribution and $\mu_{int.\,sen}$ and $\sigma_{int.\,sen}$ be from the intelligent

sensor distribution. Then, the hypotheses test for statistically comparing these distributions are:

$$H_0 : |\mu_{ref} - \mu_{int.\ sen}| = 0$$

$$H_1 : |\mu_{ref} - \mu_{int.\ sen}| \neq 0$$

and

$$t_{l-1} = \frac{|\mu_{int.\ sen} - \mu_{ref}|}{\frac{\sigma_{int.\ sen}}{\sqrt{l}}} \tag{3.15}$$

If $t_{calculated} < t_{critical}$, then we accept the null hypothesis, meaning the two distributions are statistically identical. Otherwise, the null hypothesis will be rejected.

4. In addition, we will compare the intelligent sensor estimations to the estimations obtained from the motion model using the ground truth values. The comparison process will be identical to the step 2 and 3, meaning we will construct the motion model distribution, and compare it to both the reference, and the intelligent sensor. The goal of this step is to better understand the contribution of the motion model error in the overall error of the intelligent sensor.

While this validation procedure assesses whether the distribution of the reference sensor and intelligent sensor measurements are statistically different from each other, it does not provide much insight regarding the shape similarity of the measurement curves. Fig. 3.6 illustrates this with an example in which, two observations have approximately similar shapes but they are not aligned in the global coordinated due to a translation offset. The validation procedure will clearly reject the null hypothesis; yet, the overall curves have similar shapes. For this reason, it is critical to analyze the shape similarity between the shapes of the measurement curves to have a better understanding of the intelligent sensor's behavior. We investigate the shape similarity of the two observations by using the derivative dynamic time warping (DDTW)

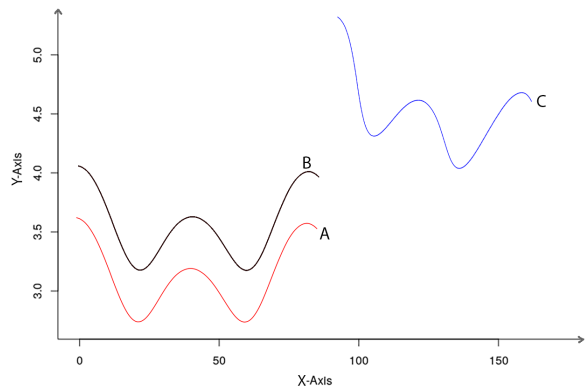

Figure 3.6: A graphical depiction of a 2D scenario in which three trajectories A, B and C have approximately similar shapes, but different locations. Assuming the curve A denotes the reference, comparison of the mean distance between A and B or A and C will yield a pessimistic measure of similarity between these three curves, illustrating the necessity of shape similarity comparison.

algorithm [76]. DDTW algorithm calculates a shape similarity score for two time series (or trajectories) which are similar, but not exactly the same. The basis of the DDTW algorithm is founded on the computation of a distance matrix between two time series. Assume $P = \{p_1, p_2, ..., p_n\}$ and $O = \{o_1, o_2, ..., o_m\}$ represent two sets of time series measurements. Then, the distance matrix for these sets is a $n \times m$ matrix in which the element $E_{i,j}$ is defined [76] as:

$$E_{i,j} = (D_{P_i} - D_{O_i})^2 \tag{3.16}$$

where

$$D_{P_i} = \frac{(p_i - p_{i-1}) + ((p_{i+1} - p_{i-1})/2)}{2} \tag{3.17}$$

$$D_{O_i} = \frac{(o_i - o_{i-1}) + ((o_{i+1} - o_{i-1})/2)}{2} \tag{3.18}$$

Using the distance matrix, the DDTW score is calculated [76] recursively by:

$$DDTW_{i,j} = E_{i,j} + \min\{DDTW_{i-1,j-1}, \quad DDTW_{i-1,j}, \quad DDTW_{i,j-1}\} \tag{3.19}$$

Using the DDTW score, the steps to compare the performance of the proposed sensor are as follows:

1. Constructing the reference DDTW distribution: Using M_{ref} and M'_{ref} observations of the reference sensor, the overall DDTW score $DDTW_{ref}$ for each observation is calculated by averaging the DDTW score of the planar projections of the points, denoted by d_x, d_y, d_Z:

$$\overline{d}_{obs_n} = \frac{\sqrt{d_x^2 + d_y^2 + d_z^2}}{3} \tag{3.20}$$

   Then, the reference DDTW distribution of K observation have the mean $\overline{d}_{ref}$ and variance σ_{ref}:

$$\overline{d}_{ref} = \frac{1}{k}\sum_{n=1}^{k}\overline{d}_{ref} \tag{3.21}$$

$$\sigma_{ref} = \sqrt{\frac{1}{k}\sum_{n=1}^{k}(\overline{d}_{obs_n} - \overline{d}_{ref})^2} \tag{3.22}$$

2. Constructing the motion model and the intelligent sensor DDTW distribution: the motion model and the intelligent sensor DDTW distribution will be obtained through the same process as the previous step.

3. Using the t-test analysis we will compare the reference, motion model and the intelligent sensor DDTW distributions.

It is important to note that the explained validation process assumes normality of the reference and test distributions. However, the results distributions may not be normal. Therefore, in addition to the t-test, we will compare the results using the following non-parametric tests:

- Kolmogorov-Smirnov (K-S) test: This test compares the shape of two sample distributions by calculating the largest absolute differences of their cumulative distribution functions (CDF) [77]. This test compares the shape of two sample distributions by calculating the maximum absolute differences between the cumulative distribution functions (CDF). Using this test, the null hypothesis states that the two distributions are sampled from the same population distribution. A small P-value will reject the null hypothesis, indicating that two sampled distributions were sampled from different distributions.

- Mann-Whitney U-test: This test compares the differences between two non-normal independent distributions, which are either continuous or ordinal [77]. Using this test, the null hypothesis is the difference between the median of two sample distributions is equal to zero. Rejecting the null hypothesis will indicate that one population tends to have either smaller or larger values than the other one.

3.2 Experimental Outline

So far in this chapter we have presented the motion model and evaluation procedure of the intelligent fiber optic senor. In continuation, we provide experimental proof that when a multimode fiber deforms, generated speckle patterns contains deterministic information to estimate the the magnitude and direction of deformation. In this approach each speckle pattern is treated as a unique combination of structure and texture. We utilize deep learning models to analyzing the structure of the speckle field as fingerprints and to extract directional information. The following experimental steps provide a systematic approach for position estimation:

1. Specklegram analysis to investigate the unique correspondence of speckle patterns to a multimode fiber optic deformation in multiple planes of motion. In addition, we provide computational models to extract the fiber optic deformation parameters from speckle patterns.

2. Estimation of sensor's heading direction from the deformation of its tip. The

results of the previous experiments provides a set of "directional hints" for the tip of the intelligent sensor. In these experiments we present a data-driven approach to learn the the relationship between the deformation of the fiber's tip and the rotation of the sensor body, using large amount of data. These experiments will provide insights into the physical behavior of the sensor, which is a required step to develop the intelligent sensor's computational pipeline.

3. Developing the intelligent sensor's computation pipeline: We provide a computational pipeline to measure of the displacement of the fiber optic intelligent sensor in according to the a motion model described in section 3.1.1. The model will calculate the transfer parameters and update the position of the sensor accordingly. Also, we validate both the sensor's motion model as well as its performance in comparison to a reference electromagnetic tracking sensor.

3.2.1 Experimental Setup

The data acquisition setup is shown in Fig. 3.7. To collect repeatable data a pendulum-based apparatus was utilized to construct a comprehensive dataset for studying the association between speckle patterns and deflection of the tip of a multimode fiber in multi-direction. The sensing transducer consists of a multimode fiber ($5.5cm$ length, $50\mu m$ core, and 0.22NA) where one end was coupled to a laser module (ThorLabs HeNe $633nm$) and the other open end was free to move toward a diffused surface. A high frame rate video industrial camera (Basler ace acA800-510um) equipped with a magnifying lens (4mm, f1.8) was placed at a distance of 1 cm and an angle of $0°$ in respect to the diffuse surface. These specs was selected to cover the entire speckle field. The camera was capable of capturing up to $511fps$, however, we noticed in preliminary tests that frame rates higher that $115fps$ adds statistically similar speckle patterns images to our dataset. Thus, the capturing frame rate was set to $115fps$. To collect repeatable data, the transducer was mounted on a pendulum.

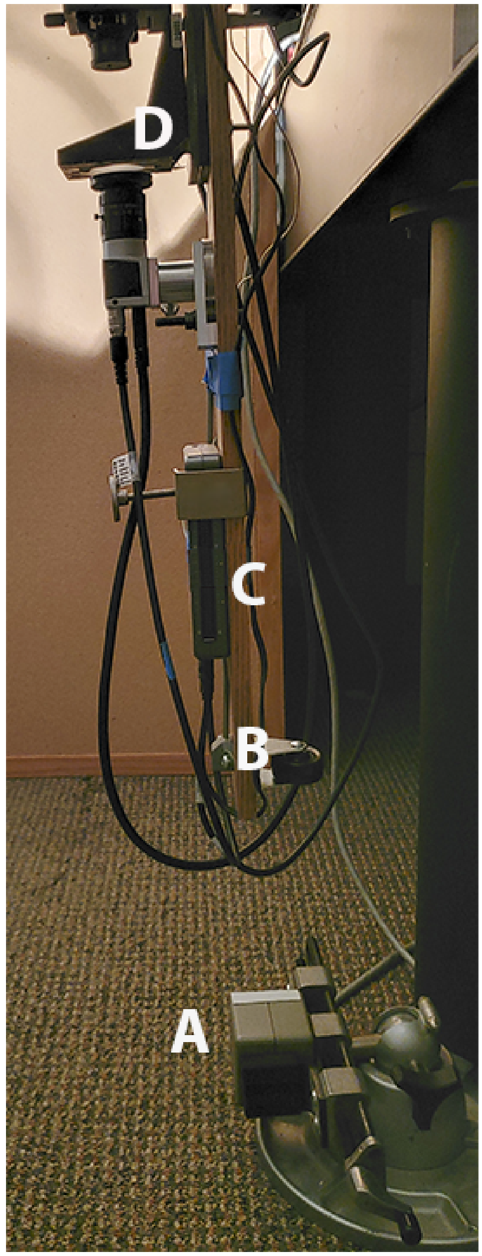

Figure 3.7: The pendulum data acquisition setup. This system includes a MMF, a diffuse surface and a high frame-rate camera (D), an accelerometer (C), and a tracker sensor (B). Estimations of the tracker sensor are in respect to its transmitter base (A). Using this setup, synchronized pairs of speckle pattern images and motion parameters were collected during the pendulum's oscillation.

To control the direction of deflection, this pendulum was mechanically restricted to move only in the xy plane. Also, we attached the pendulum to a vibration isolated table to minimize the effect of external vibration. This setup provides a framework for defining fiber's deformation in terms of a measurable quantity. As the pendulum oscillates, a restoring gravitational force $F = mgsin(\theta)$ accelerates it back toward the resting position. Here, θ denotes the rotation angle of the pendulum in respect to its equilibrium position. According to the first law of Newton, or the law of inertia:

$$F = mgsin(\theta) = ma \tag{3.23}$$

meaning under the influence of an external net force, the fiber goes under acceleration. According to the small deflection theory, for relatively small deflection of an elastic object, the amount of the deformation Δl is directly proportional to the deforming force [78]:

$$F = K_{eff}\Delta l \tag{3.24}$$

where K_{eff} is a positive constant unique to the material of the elastic object. Considering both (3.23) and (3.24):

$$ma = K_{eff}\Delta l \tag{3.25}$$

Since m and K_{eff} are constant values:

$$\Delta l \propto a \tag{3.26}$$

According to (3.26) under the influence of an external net force, the fiber's deformation is proportional to the acceleration. In other words, as a fiber optic cable experiences acceleration, variation in a fiber deformation can be expressed by acceleration vectors. To record acceleration, we used a three-axis Microelectromechanical

(MEMS) accelerometer (±8g range, $12bits$ resolution, $800S/s$ max sample rate, 3.9 mg_{rms} noise at 25Â°) next to the sensing fiber. To track the position of the transducer, we used a position tracking sensor (FASTRAK®). This position tracker will be referred as 'the reference sensor' throughout this study. Also, our experiments required a precise synchronization between the captured speckle frames and the readouts of the tracking sensor. In other words, we needed to ensure that each speckle frame and its associated deformation data were captured exactly at the same time. Therefore, we used a function generator instrument (NI-myRIO) to provide a custom triggering signal (115 pps). The camera, the accelerometer sensor and the reference tracker were set to operate in the triggering mode and connected to the function generator. With this configuration, the rising edge of each pulse triggers the acquisition of one synchronized pair of speckle pattern and the other sensors in real time.

Finally, the sensing transducer was mounted inside a rotator unit to rotate the transducer along its central axis allowing us to control the deflection direction without having to move the pendulum. As the pendulum oscillates, the deformation direction of the fiber tip aligns within the in-plane displacement of the pendulum. Therefore, by rotating the transducer around its central axis, the direction of deformation will change to a new axis accordingly.

3.2.2 Data Collection Process

The steps to construct the speckle pattern dataset were as follows:

1. Initialization of the camera and the other sensors, adjusting the rotation gauge to 0 degree, and capturing a collection of speckle images while the system is stationary.

2. Setting the pendulum into motion, and activating the triggering signal to record synchronized pairs of data. Periodically a small force was applied to the pendulum so it could maintain its swing amplitude. Once sufficient data were col-

lected, the triggering signal was deactivated, and the pendulum was returned to its initial non-oscillating status.

3. To simulate the movement in other directions, the transducer was rotated clockwise by $\alpha \in (15, 30, 45, ..., 165)$ degrees. One speckle image was captured while the system was stationary. This image was rotated the by $-\alpha$, and compared to a few random samples obtained in step 1 to ensure structural similarity $\geq 99\%$.

4. Starting from the step 2, the data collection process was repeated to cover all axis.

To account for the speckle pattern fluctuation, the data collection step was spread out over a five day period. This approach increased the variance in the data allowing the deep learning models to learn robust features during the training. Also, the reference tracker sensor was re-calibrated prior to each round of data collection to reduce bias. At the end of the data collection step, our set had 98,300 samples of paired samples separated into 13 groups according to the axis of movement (corresponding to the twelve α values plus one group of data collected while the system was stationary).

3.2.3 Pre-processing Data

To reduce the dark region surrounding speckle filed, all images were cropped from 450 x 450 pixels to 420 x 420 pixels. Then, images were converted to gray-scale images and down-sampled to 300 x 300 pixels. Finally, we applied a Gaussian blur filter and normalized the images. Our previous experiments [79] suggests while these processing steps reduces the model (number of trainable parameters), they have negligible effects on the performance. Next, speckle patterns in each group of data were assigned a label corresponding to the fiber direction of deflection in respect to its central resting position (i.e. 0 or 180 for the 0° axis, 15 or 195 for the 15° axis, etc). The total number of generated labels was 25 (24 + center), shown in Fig. 3.8. Finally, from each group an equal number of 3,918 samples were randomly selected (without replacement) and

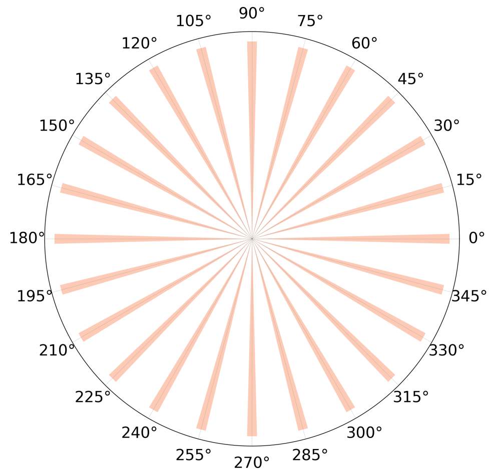

Figure 3.8: Each speckle pattern was assigned a label corresponding to the fiber's direction (axis) of deformation.

merged together. Our final dataset had total of 97,950 samples.

CHAPTER 4: SPECKLEGRAM ANALYSIS

In chapter 3 we provided an overview of the intelligent sensor's schematic, motion model as well as a validation procedure to evaluate its performance. We also explained a pendulum-based apparatus to construct a comprehensive dataset for studying the association between speckle patterns and deformation parameters of a multimode fiber (MMF). This chapter provides a series of experiments to illustrate the feasibility of utilizing speckle pattern analysis for position estimation. To avoid redundancy, the terms 'deformation' or 'bending' will indicate 'deformation of a multimode fiber optic cable'.

4.1 Estimation of the Direction of Deformation

In this work, by using a supervised learning approach, we show that in a deforming multimode fiber, structural variation of speckle patterns contains deterministic information for measuring the direction of deformation. As an elastic medium, an optical deforms under the influence of external forces and returns to its initial status when forces are removed. Given a series of speckle images $I_{1 \to n}$ corresponding to K distinct axis (direction) of deflection ($2 \leqslant K \ll n$), our objective is to estimate a mapping function such as f where $k \approx f(I_i)$, $k \in K$ and i corresponds to the I_{ith} frame. The mapping function is represented by a CNN model. Through training, the model learns the unique structural and textural information that corresponds to each of the k classes, and encodes them into a feature spaces. Given such a mapping function, one can iterate over series of speckle patterns images and extract directional information. We conducted two experiments to analyse the influence of the direction of deformation on the speckle pattern structure:

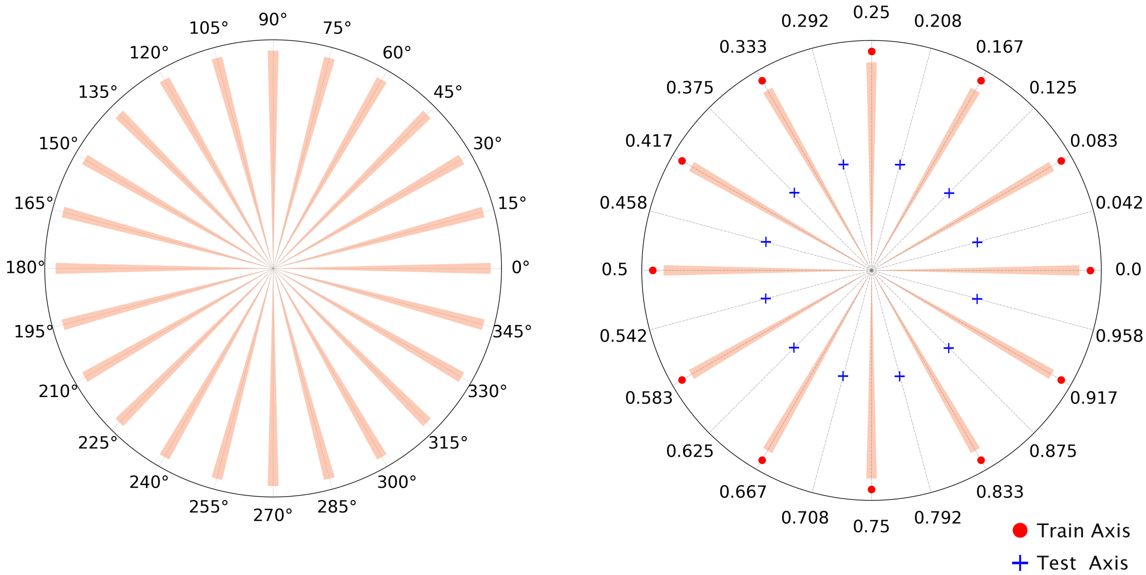

Figure 4.1: In the second experiment, the directions were mapped to equal values $\in [0, 1)$. A deep learning was trained using the samples from the 0, 30, 60,..., 330 directions, and then, evaluated using the unseen samples from the 15, 45, 75,..., 345 directions.

1. In the first experiment, we examined the deterministic nature of speckle patterns for extracting directional information. The dataset was shuffled, and training and test sets were generated by splitting the dataset into 85/15 train/test ratio. Also, 20% percent of the training set was used as the validation set. A CNN model was trained to learns the mapping between the speckle pattern images and their corresponding labels using the train set. Then, the performance of the model was evaluated using the test set. We hypothesised that if speckle patterns exhibit a deterministic nature, the network will identify the correct direction classes for the test set unseen images.

2. In the second experiment, we approach the problem from a regression perspective to investigated whether a trained model can estimate the direction of deformation using unseen speckle images (novel data), as shown in Fig. 4.1. Similar to the first experiment, we generated a labelled set to create a nonlinear mapping from speckle images to the direction of deformation. The train set

was consisted of sample pairs corresponding to the 0, 30, 60,..., 330 directions and the test set had all samples from 15, 45, 75,..., 345 directions. The portion of data taken when pendulum was stationary was not used in this experiment. Then, labels were mapped from 0 to 360 degrees to equal values between 0 and 1. We trained the model to learn the deformation axis for the speckle images in the training set. Then, the ability of the model in estimating the deflection direction was evaluated by using unseen images from the test set.

4.1.1 Architecture of the Deep Learning Model

CNN is a deep learning architecture which is inspired by the biological model of the visual cortex. They have achieved excellent performance on recognition of complex visual patterns. What makes a CNN unique is their ability to identify non-linear relationships in the data. Here, we use a CNN model to learn the one-to-one mapping of speckle patterns to the direction of deflection. As represented in Fig. 4.2, our model has a classic convolutional architecture of five convolutional layers to extract features, three fully-connected layers to learn the patterns, and one output layer to provide prediction or estimation. Our motivations for this CNN model was to utilize a relatively small number of layers (and thus, parameters) to reduce the training time as well as overfitting. Convolutional layers extract features into a feature map. Each convolutional layer has multiple filters which their values are learned during the training. The output of each convolutional layer is a set of two dimensional feature maps such as I_K where

$$I_k = RELU(W_k * X + B) \tag{4.1}$$

where W_k and B are weights and bias associated with filter K, and * is convolutional operation, and $RELU$ is the rectified linear unit $RELU(X) = MAX(0, X)$. By applying activation function, CNN model can exploit both linear and non-linear patterns. We used relatively small kernel for our filters (5 and 3) since speckle pat-

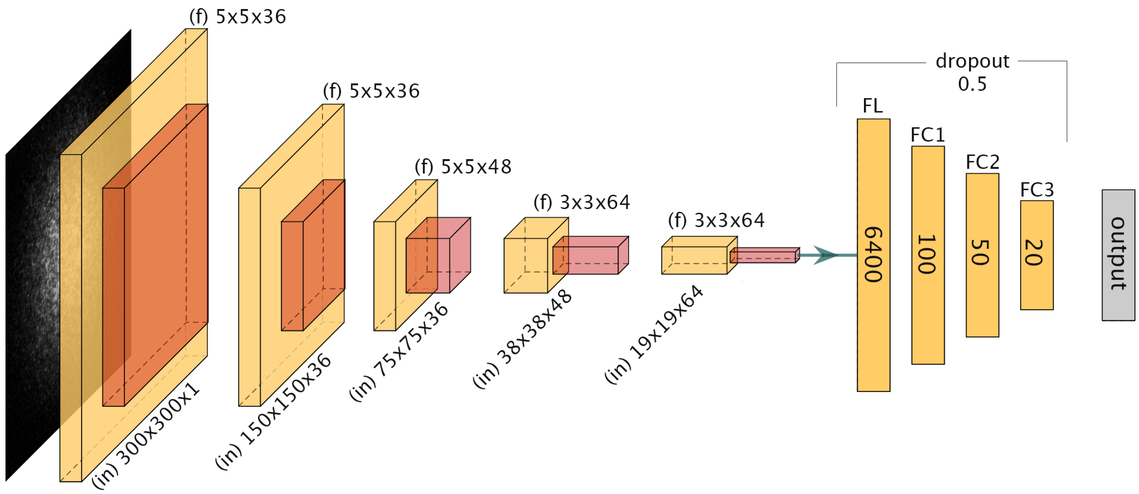

Figure 4.2: Architecture of the CNN model according to this work. The input is a batch of 300 x 300 grayscale images, which is passed through five convolutional layers. The input size, and the kernel size for each convolution layer are denoted by (in) and (f), respectively. All convolution units have the stride length of two. The output layer provides 25 prediction scores in the first experiment, and one estimated value $\hat{y} \in [0, 1)$ in the second experiment.

terns were condense. As we will demonstrate in result sections, these small size filter sizes are sufficient for this learning task. After the last convolutional layer, feature maps are flattened to a one dimensional vector and passed to the dense layers for further processing. Dense are similar to traditional neural network where neurons of consecutive layers are fully-connected. Each dense layer included a dropout regularization to further reduce overfitting. The output layer in the first experiment was a 25-neurons dense layer providing 25 classification scores.

In the second experiment, the output layer contained one neuron for regression estimation. The number of trainable parameters were 787,955 and 787,451 for the first and second experiments, respectively. The initial learning rate was set to 0.0001. The model was implemented using TensorFlow 1.14, and it was trained using an Nvidia graphic card (GeForce 1070-Ti, 2432 cuda core, 8GB GDDR5).

Table 4.1: Assessment of classification performance using the test dataset.

Labels(Axis)	Precision	Recall	F1-score	Support
center	0.95	0.96	0.95	753
0	0.96	0.96	0.96	749
15	0.98	0.95	0.97	809
30	0.94	0.99	0.96	739
45	0.93	0.97	0.95	726
60	0.97	0.93	0.95	787
75	0.97	0.96	0.96	799
90	0.99	0.94	0.96	807
105	0.95	0.97	0.96	803
120	0.98	0.93	0.95	825
135	0.96	0.96	0.96	762
150	0.97	0.95	0.96	763
165	0.97	0.95	0.96	850
180	0.96	0.96	0.96	795
195	0.95	0.98	0.96	757
210	0.99	0.94	0.96	823
225	0.97	0.94	0.96	819
240	0.93	0.97	0.95	770
255	0.96	0.97	0.96	756
285	0.97	0.94	0.96	799
300	0.92	0.98	0.95	773
315	0.96	0.96	0.96	770
330	0.95	0.97	0.96	791
345	1.00	1.00	1.00	756
Average	0.96	0.96	0.96	
Total Samples				19,575

4.1.2 Evaluation of the Deep Learning Model

The goal of the first experiment was to examine the deterministic nature of speckle patterns shape and structure in respect to deformation direction of a fiber tip. The CNN model was trained on 62,675 samples for 30 epochs with using a batch size of 30 samples. The training process was completed in less than an hour. The trained model was tested on sets of 19,575 speckle images. For each label, True Positive (TP), False Positive (FP), True Negative (TN), and False Negative (FN) were identifed. We used the the following metrics to evaluate the performance of out model: precision

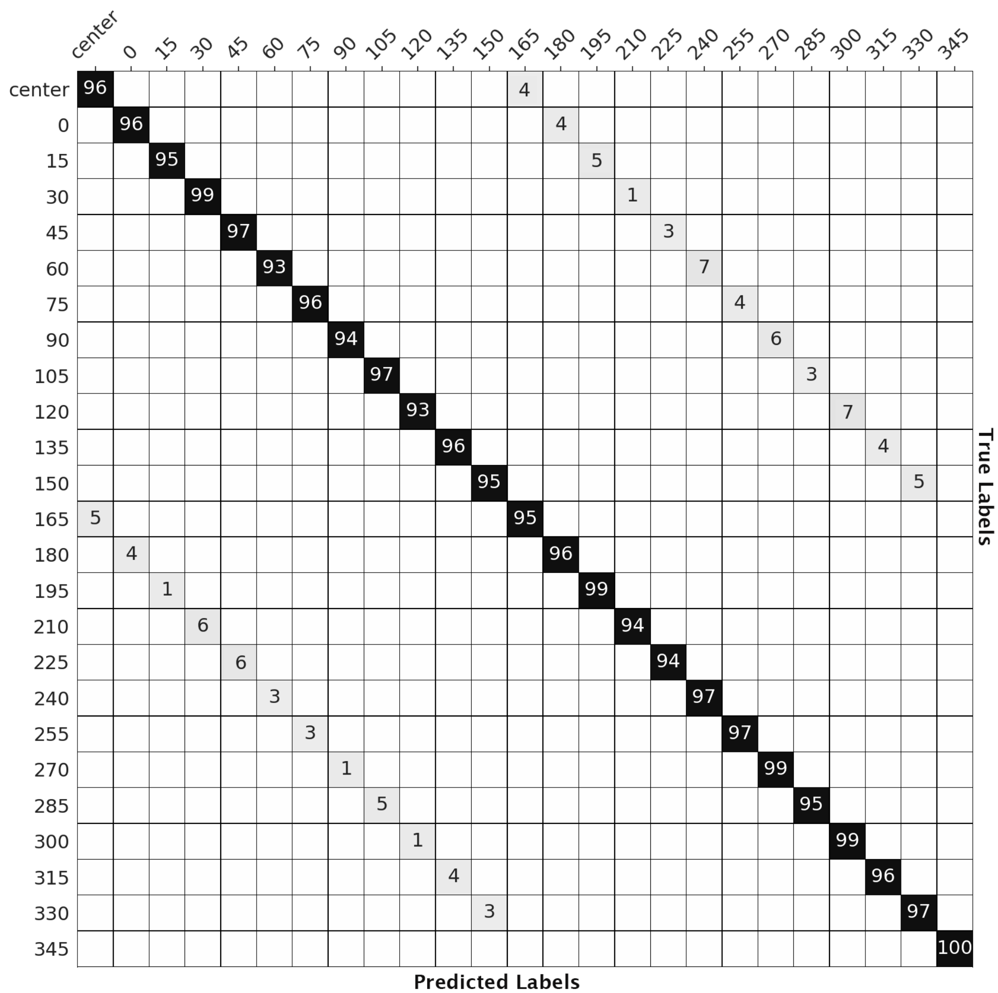

Figure 4.3: Each row of the matrix corresponds to an actual class (a True label), and each column corresponds to a predicted label. Numerical values represent percentage values between 1 and 100, and empty cells indicate 0%. The diagonal blocks represents the percentage of correctly classified labels. Cells are color codded: higher the accuracy, darker the color.

(TP/TP+FP), recall (TP/TP+FN), accuracy, F1-score ($2 * \frac{precision*recall}{precision+recall}$).

Table 4.1 provides a comprehensive overview of the model performance for each axis label. The model achieved overall 96% accuracy. The minimum precision, recall, and F1-score were 92%, 93%, and 95% respectively. Fig. 4.3 shows the visualization of the confusion matrix to to have a better picture of the performance of the model. In confusion matrix, the diagonal represents the elements where the predicted values were equal to the expected values. Similarly, the off-diagonal cells are the sample

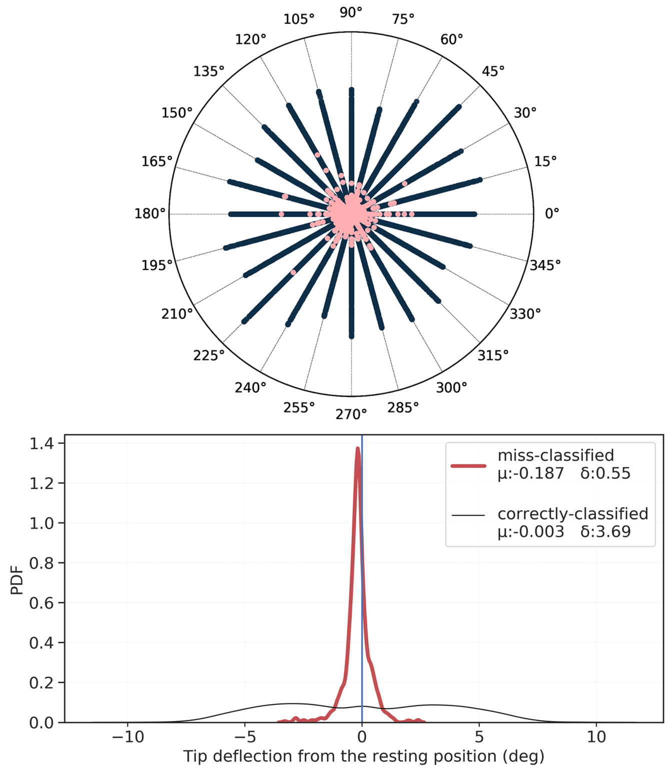

Figure 4.4: (Top Figure) Projected deflection of the fiber's tip for the correct (dark) and incorrect (bright) classified samples. (Bottom Figure) Distributions of tip of the fiber deformation for both groups. The zero vertical lines indicates the resting position. Miss-classified samples tend to be clustered around the center, i.e. the fiber's resting position.

instances which are miss-classified by the model. The strong diagonal shape of the matrix confirms the high accuracy of the classification model.

More careful observation of the confusion matrix (Fig. 4.3) shows that the larger confusion is presented among samples which are located on the same axis, but opposite directions (i.e.: 0 vs 180). The reason for this confusion becomes more clear by comparing the fiber deformation distribution of the correctly classified speckle images with mis-classified samples (Fig. 4.4). The deformation distribution of incorrectly classified speckle images have a $\mu = 0.0$ and $\sigma = 0.06$ meaning that these samples were taken when the tip of the fiber was close to the resting position, and the direction of deformation was about to be switched to the opposite direction. The possible explanation for this errors is de-synchronization of speckle pattern and the mapped

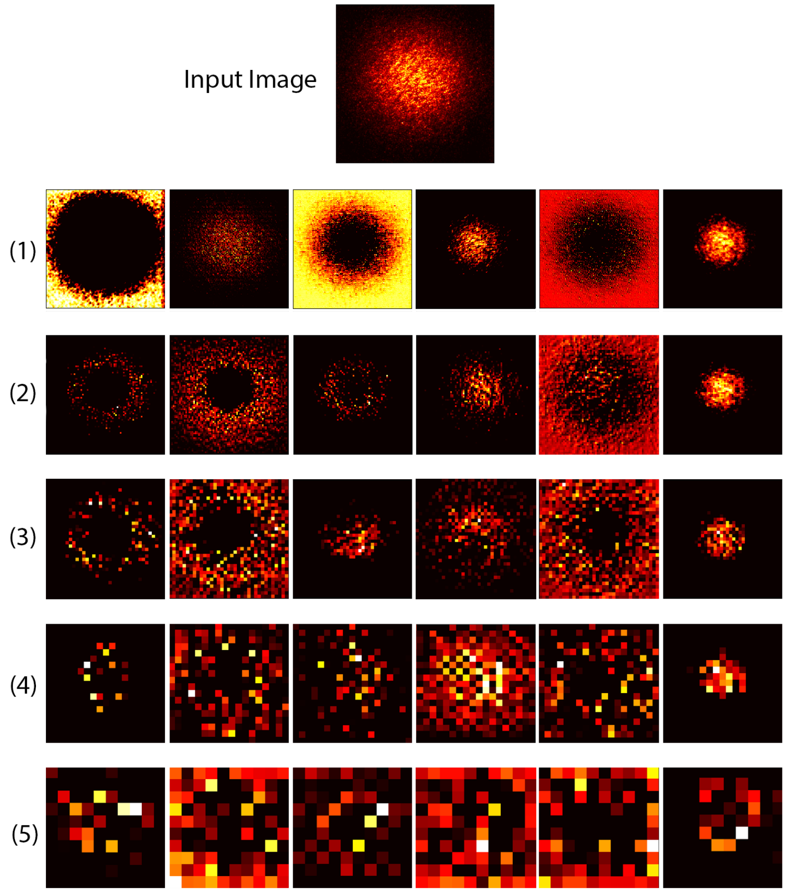

Figure 4.5: Visualization of the activation maps extracted from the convolutional layers. The images within each row are extracted from the same layer, which are indicated by the numbers 1 through 5. We can see that the feature maps closer to the input of the model, i.e. layer one and two, capture the overall structure of the input speckle pattern. As we progress deeper into the model, the feature maps show less and less recognizable information. However, the extracted details of the last two layers are more relevant to the predictions of the model.

axis of deformation dusting the data collection process. Applying a more precise calibration process may reduce this type of error.

Visualizing the activation maps provides insights about the behavior of our model by identifying the most relevant sections of input images to the final prediction of the network. One common practice for visualization of activation map is to feed a test image into the trained model and plot the context of convolutional filters as 2D images [80, 81]. Fig. 4.5 represents visualization of some of the convolution filters for each of our CNN model. During training, the filters in the first convolutional layer seems to respond to the cluster of dark and bright regions of the input speckle images representing highly recognizable visual contents such as dark background, central region with where the intensity if maximum, and overall structure of the speckle pattern. One can also see that the activation maps of the first two layers are more visually interpretable. As we go deeper into the model, the resolution decreases, activation maps becomes more abstract, and they tend to discover the hidden more complex patterns which are more relevant to the prediction of the model. In the other words, the outer layers of our model capture the general structure of the specklegram, and the deeper(inner) layers learn specific patterns so the model could generalize about the class and not any particular images. Overall, these results confirm that there is a deterministic relationship between the structure of speckle patterns and the direction of deflection.

In the second experiment we tested the capability of a CNN model to estimate the direction of deformation using unseen speckle patterns. First, the model was trained using the sample data corresponding to the 0, 30, 60, ... , 360 directions. Then, the model was tested using speckle images taken from the 15, 45, 75, ... , 345 directions. Note that each testing directions fall between two training directions. Since the train and test sets correspond to different deformation directions, they both had an equal size of 12*3918=47,016 samples. The model was trained for 55 epochs using a batch size of 30 samples. We used the standard mean squared error loss function, and the Adam optimizer [82] to fit and minimize the loss function. Then, the performance of the model was evaluated by comparing the model′s estimation of direction of deformation with the ground truth value.

The box-plot charts shown in Fig. 4.6 provides a comprehensive summary of the model estimation for each tested axis. The results indicated that in most cases the model estimation falls within ±5 degrees from the ground truth. This is particularly

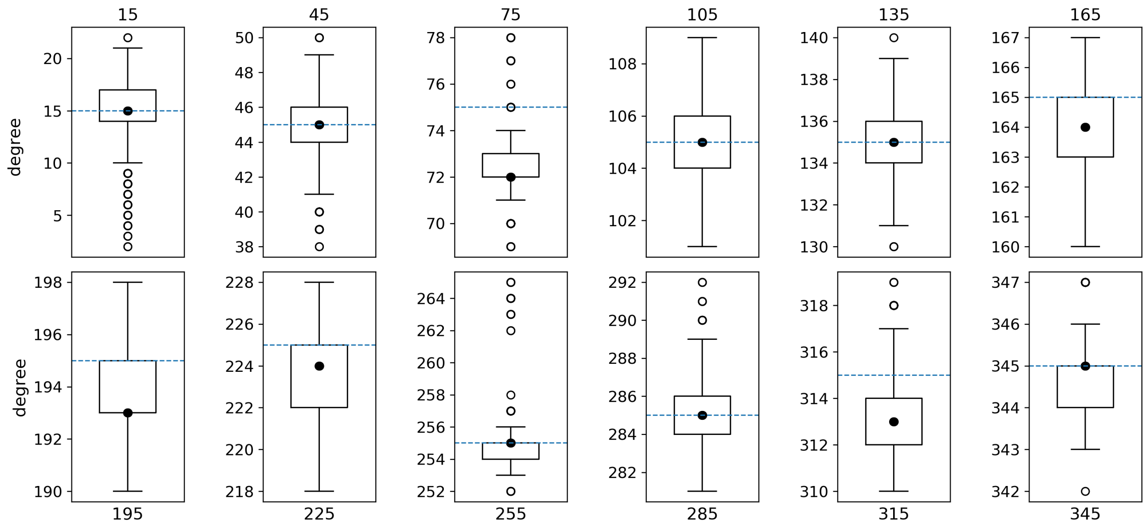

Figure 4.6: Summary of the estimated directions of deformation. In each box-plot, the dash line indicates the ground truth values.

an interesting results considering the fact that the distance between direction of deformations for training samples was 30°. This implies that for each unseen speckle image, the model determined which two directions it is between, and estimated the direction of deformation accordingly. The best results were obtained for the 45°, 105°, and 135° where the mean of the estimated value was equal to the ground truth. Yet, in most cases, at least one estimated value falls beyond the 25%-75% range. Fig. 4.7 presents the normalized probability density function (PDF) of the estimation error for each deformation direction. In this chart, each column represents two opposite directions which are located on the same axis (i.e. 15° vs 155°). These results indicates that the estimations errors are random, not following a normal distribution. Also, these errors are independent from the axis of deformation. This is inline with the previous works on speckle patterns that demonstrate speckle patterns introduce random error to the measurements. It may be possible to reduce this error by using a larger training set. These results confirm that speckle patterns shape and structure indeed contains significant information for estimation of the direction of deflection.

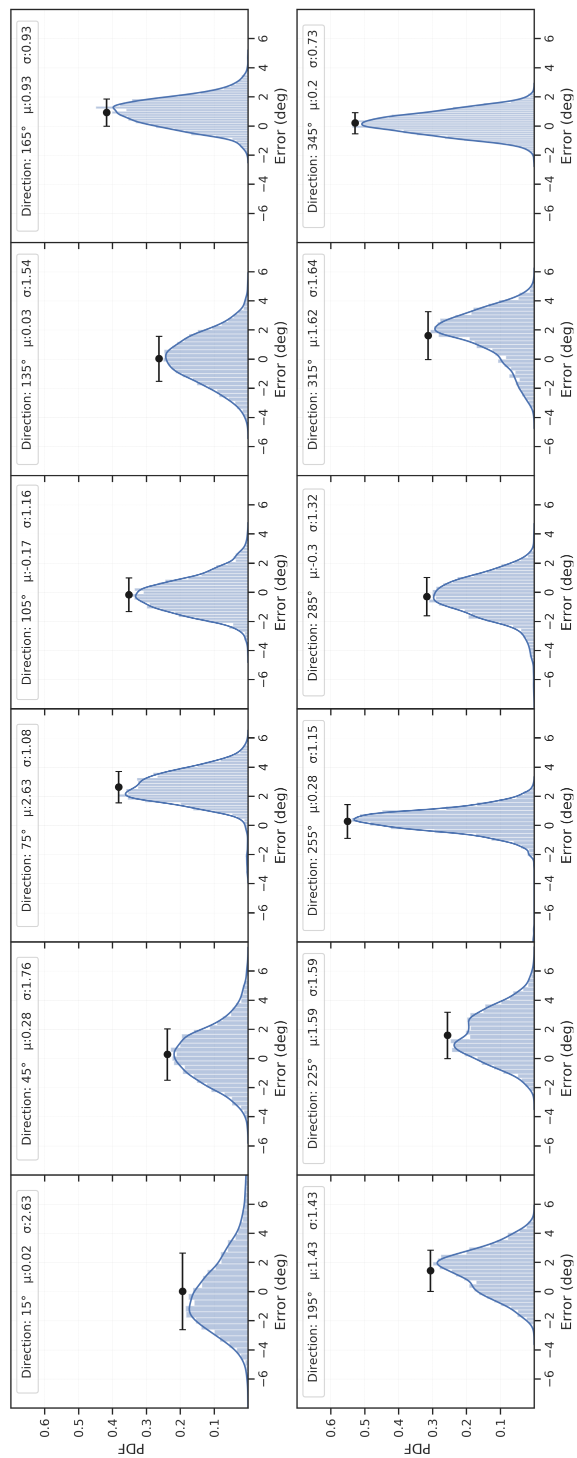

Figure 4.7: Distribution of errors of the estimated directions of deformation.

4.2 Estimation of the Deformation Magnitude

In this study, we investigated whether speckle analysis could be utilized for measuring the deformation magnitude of a fiber cable. In particular, we show that a properly trained CNN model is able to extract the best matching features of speckle patterns to estimate the deformation magnitude of a multimode fiber. Let $I_{1\to n}$ and $\theta_{1\to n}$ denote a series of speckle patterns and their associated deformation magnitudes, respectively. Our goal here is to estimate an optimal function such as $f(.)$, which maps $I_t \to \theta_t$ at time instance$t$:

$$\theta_t = f(I_t) \tag{4.2}$$

Given such a mapping function, one can iterate over series of speckle patterns images as tip of a fiber deforms, and estimate the deformation magnitude in respect to its resting position. Note that as explained in 3.2.1, deformation was expressed by acceleration vectors. During data collection, synchronized pairs of speckle pattern images and acceleration data from the reference MEMS accelerometer were recorded. To prepare data for this study, the outliers (values beyond the 5% and 95% quantiles) and their corresponding images were removed from the dataset. Then, The reference accelerometer data was normalized and shuffled. Using this dataset, we conducted two experiments to explore the use of a CNN model for estimation of a multimode fiber's deformation magnitude:

1. In the first experiment, we hypothesised that as a multimode fiber deforms, there is a one-to-one correspondence of deformation parameters to the speckle patterns variation. That means in a deforming multimode fiber, every state of the physical shape of the fiber corresponds to a unique speckle pattern. To test this hypothesis, the accelerometer data was grouped into 19 deformation classes (states), and each speckle image was assigned to one of these categorical groups, see Fig. 4.8. Then a train set, and a test set was created by splitting the dataset

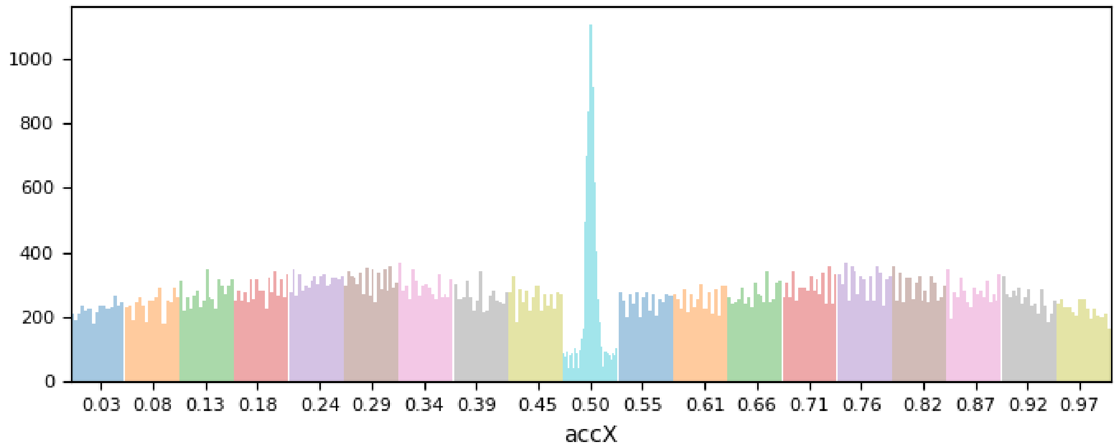

Figure 4.8: To evaluate the deterministic nature of speckle pattern, the entire acceleration range was divided into 19 distinct classes. A CNN model was trained to learns the mapping between the speckle patterns and their corresponding acceleration groups.

into 80/20 train/test ratio. Also, 20% percent of the training test was used as the validation set. The total number of samples in the train set, validation set, and test set were 61,044, 15,262 and 19,077 respectively. A CNN model was trained to learns the mapping between the speckle pattern images and their corresponding labels using the training set. The architecture of the CNN model was identical to the previous study (see Fig. 4.2) with the exception of the last layer. The output layer in the this experiment was a 19-neurons dense layer providing 19 classification scores. Then, the performance of the model was evaluated using the test set. If speckle patterns exhibit a deterministic nature, the network will correctly identify the deformation classes for unseen specklegrams.

2. In comparison to the previous experiment, in the this experiment our goal was to estimate the deformation magnitude on a continuous scale rather than categorical labels. In particular, a CNN was used as a regression models to discover feature correlation between speckle pattern images and the deformation mag-

nitude on a continuous scale. We used the same train, validation and test sets as the previous experiment. However, instead of the acceleration labels, the normalized acceleration values values were used as the target variables. The architecture of the CNN model was similar to the model used in the previous study. The only modification was using an one-neuron dense layer for regression estimation. Once the model was trained, its performance was evaluated by using unseen images from the test set.

4.2.1 Experimental Results

In the first study, we investigated the deterministic nature of speckle patterns for estimating deformation magnitude. The CNN model was implemented using TensorFlow 1.14, and the initial learning was set to 0.001. Also, categorical cross-entropy loss was used to train the model. After the training, precision, recall, F1-score, and overall accuracy was used to evaluate the model.

Overall, the experiment results confirmed the initial hypothesis, that, there is a one-to-one correspondence of deformation parameters to speckle patterns. The performance of the model during the training phase is presented in Fig. 4.9. The model achieved above 97% accuracy after 150 epoch without overfitting problem. Table 4.2 presents a detailed precision and recall summary of the classification performance for each label; The minimum precision, recall, and F1-score were 90%, 90%, and 91% respectively. Fig. 4.10 presents the visualization of the confusion matrix that was made based on this table. The strong diagonal shape of the matrix confirms the high accuracy of the classification model. These results indicates that the model is effective for all deformation classes, or the entire range of the fiber deformation.

The possible explanation for the errors with relatively small magnitude is desynchronization of speckle pattern and the mapped value dusting the data collection. This type of error can be reduced by improving the instrumentation and data collection procedure. Another factor that may contribute to errors with a large magnitude

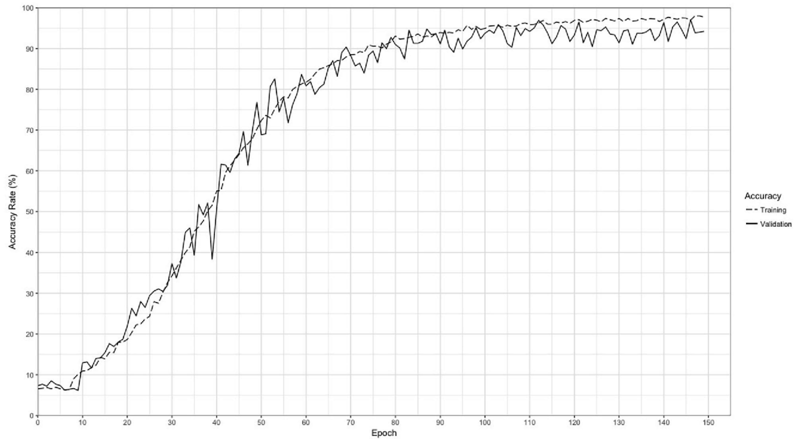

(a) Trend of training and validation accuracy rates

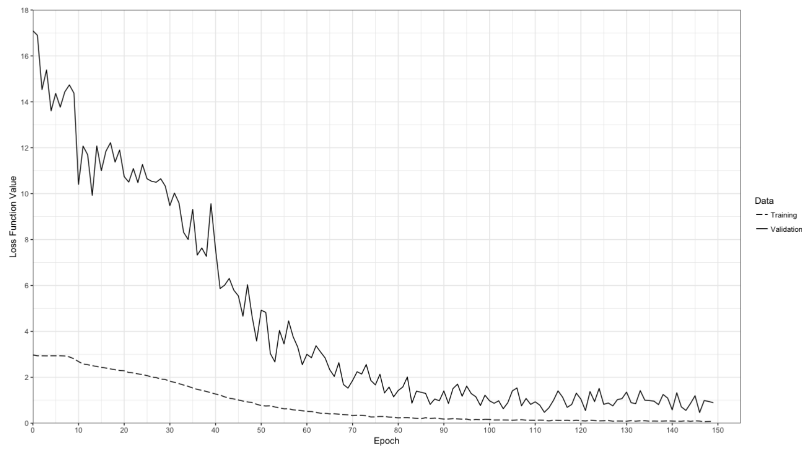

(b) Trend of the loss function value.

Figure 4.9: (a) Training the model for 80 epochs is sufficient to achieve 90% accuracy. Accuracy of 97% was achieved by training the model for 150 epochs. (b) The loss function for training and validation decreases quickly during the first 70 epochs and converges to minimum by the 150th epoch.

is the similarity between the speckle patterns in those states. That means although speckle patterns are not quite identical, they share more than average similarity that is not detectable by our model. These results confirms that the speckle patterns provide information that could be used to estimate the deformation of a multimode fiber cable.

The goal of the second experiment was to estimate the deformation magnitude of a multimode fiber through speckle analysis. We trained a CNN model as a regressor to find the best fit between the fiber's deformation magnitudes and the non-linear

Table 4.2: Classification results for each label

Labels	Precision	Recall	F1-score	Support
-1.9	1.00	1.00	1.00	1056
-1.7	1.00	1.00	1.00	1038
-1.5	0.99	0.96	0.97	1129
-1.3	0.98	0.99	0.99	953
-1.1	0.94	0.99	0.97	984
-0.9	1.00	0.94	0.97	1200
-0.7	0.96	1.00	0.98	916
-0.5	0.96	0.98	0.97	1010
-0.3	0.99	0.98	0.98	979
-0.1	0.98	0.95	0.96	901
0.0	1.00	0.96	0.98	1022
0.2	0.99	0.99	0.99	892
0.4	1.00	0.95	0.97	971
0.6	0.90	0.96	0.93	1125
0.8	0.92	0.98	0.95	971
1.0	0.96	0.90	0.93	872
1.2	0.92	0.90	0.91	1052
1.4	0.94	0.99	0.97	1078
1.6	1.00	1.00	1.00	928
Average	0.97	0.97	0.97	
Total Samples				19077

features of speckle patterns. The model's input and the target variable were speckle images and the normalized deformation magnitudes, respectively. The mean square error loss function and the Adam optimizer [82] with an initial learning rate of 0.0001 were utilized to train the model. We also applied transfer learning to set the initial weights of convolution layers. Transfer learning is a machine learning technique allowing deep learning models to share knowledge in similar applications, reducing the training time. The model was trained for 50 epochs using the batch size of 30 samples. After the training, the performance of the model was evaluated by comparing the model's estimation of deformation with the actual values using R-squared metrics. R-squared metrics, or the coefficient of determination is the percentage of

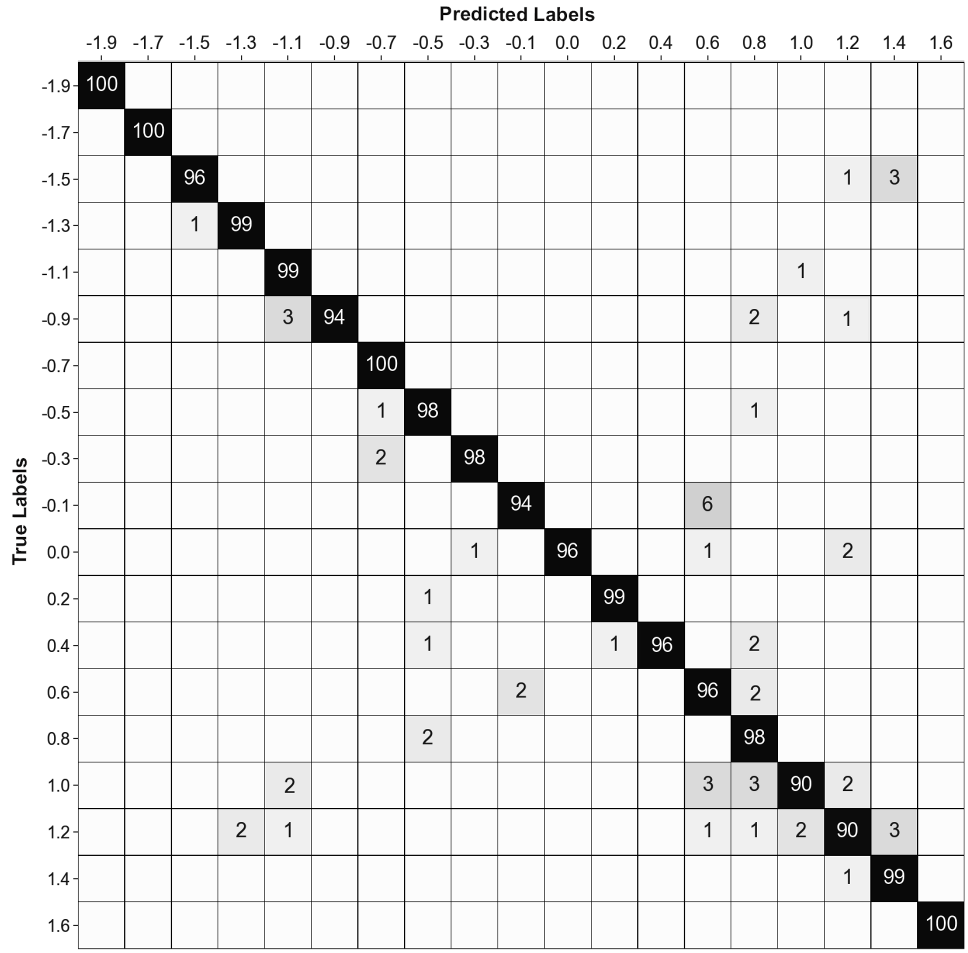

Figure 4.10: Visualization of the confusion matrix for Classification of a multimode Fiber Deformation States. Numerical values represent percentage values between 1 and 100, and empty cells indicate 0%. High classification accuracy of the CNN model is represented by the strong diagonal shape of the matrix.

the response variable that is detected by the model:

$$R^2 = 1 - \frac{MSE}{Var(y)} \tag{4.3}$$

where MSE(mean square error) represents the model's variance. For a perfect model, $MSE = 0$, and thus, $R^2 = 1$.

Fig. 4.11 provides a visualization of how well our model fitted the test data. The plot on the left panel indicates a strong correlation between the model's prediction and

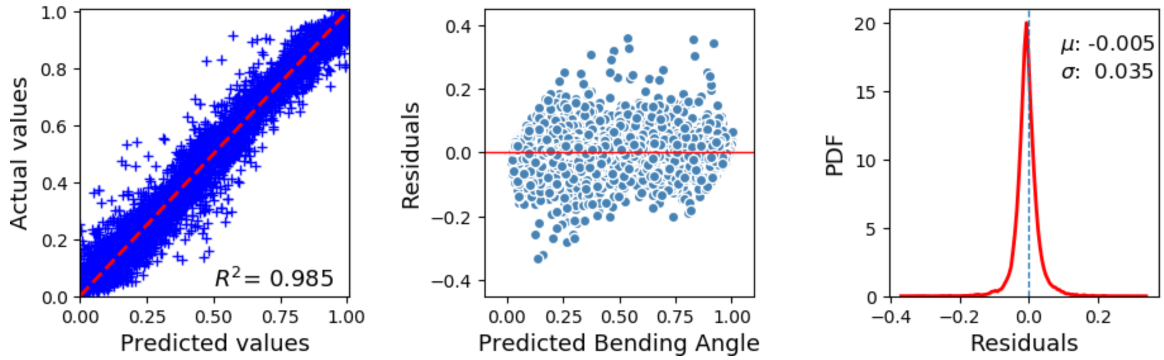

Figure 4.11: (Left Panel) Scatter plots of the actual vs predicted values showing the deviation of the predictions from the ground truth. We can see that all the points are be close to the diagonal line, indicating an effective model. (Middle Panel) The residuals vs. prediction plot demonstrating errors have equal valiance, and clustered around zero. Also, the distribution of the errors is normal, as shown in the right panel.

the actual values (R^2 = 0.985). The residual plot, Fig. 4.11(middle panel), provides a better insight into the model's performance. We can see that with the exception of a few outliers, errors are symmetrically distributed and clustered around the center line, indicating the equal variance of the errors. This is also confirmed by the distribution plot of the errors, presented in the Fig. 4.11(right panel). Fig. 4.12 presents the probability density function of the deformation estimation error according grouped by the deformation labels. We can see that for all groups, the errors are normally distributed, suggesting errors have a random nature. Random errors are primarily caused by unpredictable changes during the experiments, i.e.: laser fluctuations, noise in the measuring sensors, environmental conditions, etc. Thus, it is impossible to eliminate them. However, random errors mostly affect the precision of the measurement. This suggests at any stage of deformation, analyzing a larger number of speckle patterns will produce a more precise measure of deformation. Overall, these results provides the proof-of-concept that the specklegram structure contains deterministic information, which can be exploited to measure deformation parameters. In the next study, we use the results of these studies to measure the intelligent sensor's orientation.

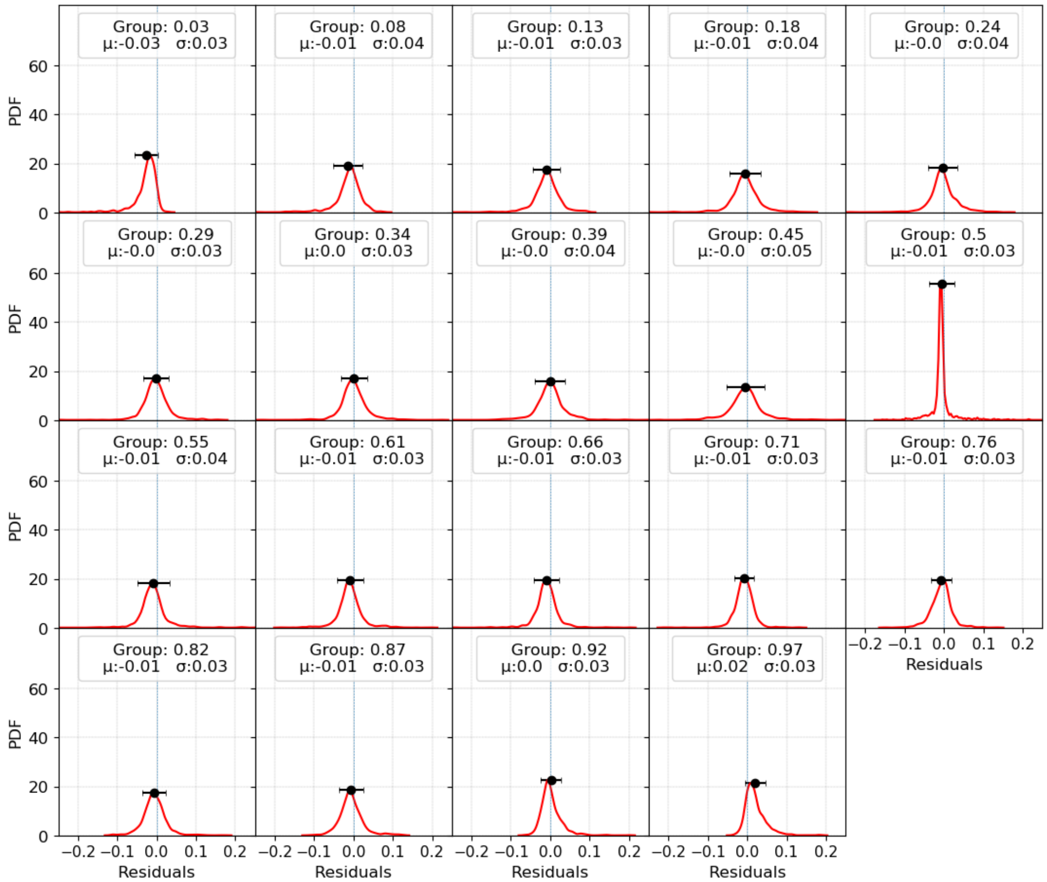

Figure 4.12: Distribution of error for the entire range of fiber deformation separated by labels.

4.3 Estimation of the Intelligent Sensor's Orientation

In the last two sections, we outlined a computational framework for deriving a multimode fiber's deformation parameters through speckle analysis. This section provides insights into the dynamic behavior of sensing transducer as a coupling of a rigid body and a flexible fiber optic. In particular, we intend to understand the relationship between the sensor's heading and the corresponding deformation magnitudes. The motivation for this study results from the fact due to the elasticity of fiber optics, factors such as vibrational noises or changes in the temperature influence their deforming behavior. This is an important issue since the accurate estimation of the intelligent sensor's heading from the fiber deformation is crucial for tracking its trajectory.

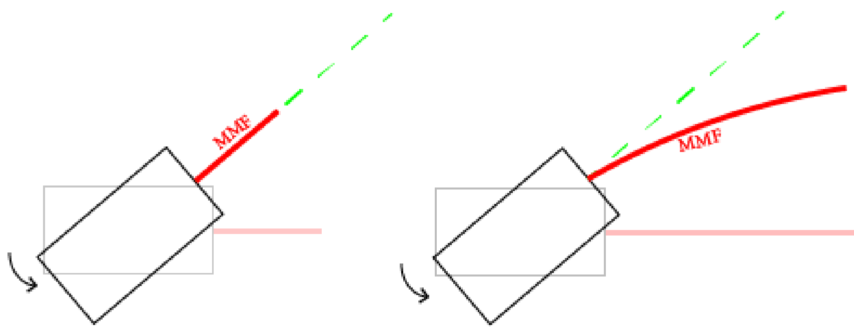

Figure 4.13: Under rotation, the length of a fiber optic segments (MMF) influences the alignment between the heading of the sensor and the position of the fiber's tip. The longer the fiber segment, the more its tip deviates from the heading of the sensor.

Fig. 4.13 presents two hypothetical design modalities for the sensing transducer. The first model employs a short segment of fiber optic, which behaves as a rigid uniform segment. As the sensor undergoes a rotation, the heading of the sensor perfectly aligns with the position of the fiber's tip. However, this is not a practical model since the magnitude of the fiber deformation is close to zero, implying a low sensitivity transducer. In comparison, the second model employs a longer segment of fiber optic. Under rotation, the fiber's tip deviates from its resting position, and thus, the senor's heading and the fiber's tip position no longer align. The degree of this misalignment is primarily affected by the fiber's oscillating behavior due to its length and elasticity. To this extend, we performed a simulation study to both observe the fiber's oscillating behavior, and to check the relationship between the sensor's rotation and the deformation of its sensing fiber tip. Using Matlab, we modeled the data collection pendulum system eliminating the laser and the camera. The equation of motion was set according to an ideal pendulum system [83]. Also, gravity was set as the main force of acting on the pendulum. To model the fiber optic, we follwed the literature suggests that the mechanical behavior of a fiber optic can be modeled as a cantilever beam [84]. In such an approach, the deformation ΔL of a clamped

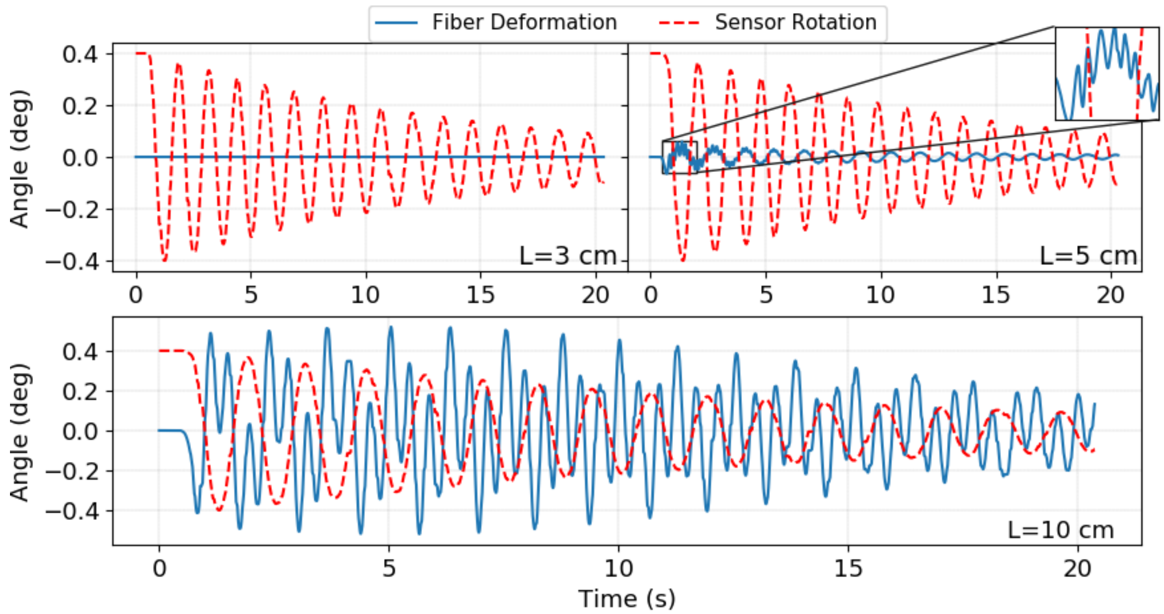

Figure 4.14: Effect of a multimode fiber length on its oscillating behavior. We can see a longer segment of fiber exhibits more drastic periodic oscillation.

optical fiber with a under acceleration a can be estimated by:

$$\Delta L = \frac{A\rho l^4 a}{8EI_{cylinder}} \tag{4.4}$$

and

$$I_{cylinder} = \frac{\pi d^4}{64} \tag{4.5}$$

where $I_{cylinder}$ is the second moment of area, A the fiber's cross-sectional area, d and l fiber's diameter and length, ρ the mass density, and E represents the Young's modulus[84]. For implementation, we used the provided flexible beam model in Matlab [85] for modeling the fiber optic segment because of this model's ability in calculating the motion dynamics of a rigid body and a flexible link. The fiber optic we used has $d = 50\mu m$ diameter. The other model parameters were set as $\rho = 220\ {}^{kg}/_{m^3}$, $E = 7.3 \times 10^{10}\ pa$ as suggested by [86]. Three rounds of simulation was performed to capture the motion parameters of the pendulum system under gravity for a 3 cm, a 5 cm, and a 10 cm fiber. The results are provided in Fig. 4.14.

These results indicate that the length of the sensing fiber optic significantly affects its vibrational behavior. While the deformation of 3 *cm* fiber was close to zero, the 10 *cm* fiber exhibited drastic periodic oscillation with varying amplitude and phase. In comparison, the 5 *cm* fiber showed the most stable deforming behavior. As expected, both 5 *cm* and 10 *cm* behaviors confirmed that the fiber's in place rotation and its deformation have opposite phase (180°). Between these results, the 5 *cm* fiber deforming behavior suggests that with proper adjustment of a fiber's length, the oscillating behavior of its tip can be used to describe the rotational characteristics of the sensor. However, this relationship is not instantaneous. In other words, the instantaneous deformation parameter does not successfully provide meaningful insights into the sensor's rotation. This confirms a well-known phenomenon, that the time-average oscillation power of a vibrating structure is more descriptive variable than its instantaneous value [87]. These results suggest learning long-term dependencies between the deformation parameters and the sensor's rotation may provide a stable and reliable solution for estimation of the sensor's rotation. One way to extract the long-term deformation features is through the application of a Long Short-Term Memory (LSTM) deep learning model.

LSTM is a special type of recurrent neural network, capable of learning temporal hidden features in data. LSTM algorithm was initially introduced in 1997 [88], and currently, due to the increase in computational power, it is the state-of-art algorithm for solving problems in which processing non-linear sequential data is required. The unique advantages of LSTM networks are three-folds. 1 - They can learn and track long-term temporal dependencies in data. 2 - The maintain information about the samples' order. 3 - They can share the learned parameters across the data samples.

In this experiment, we utilize a LSTM model to estimate the sensor's rotation through analysing sequences of deformation values. Our goal is to verify that a computational LSTM model can be trained to estimate the intelligent sensor's orientation

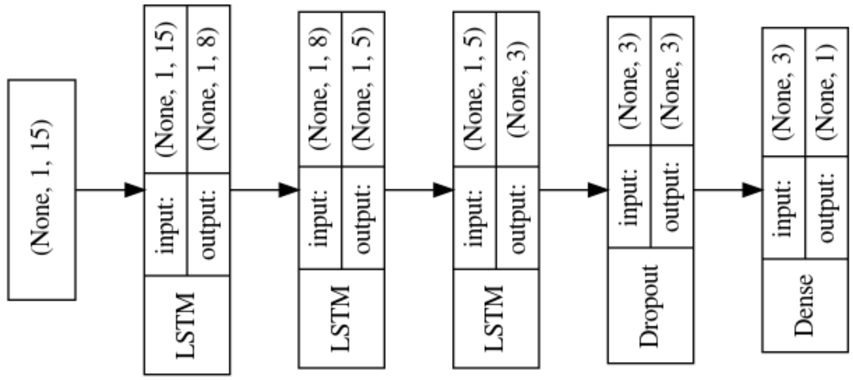

Figure 4.15: Architecture of the LSTM model according to this work. The input is batches of 1 x 15 deformation values, which is passed through three LSTM layers. The input and output shape of each LSTM layer is denoted by (input) and (output), respectively. In training or evaluation, None parameter to the batch size. The output pf this model is the estimation of the intelligent sensor's heading.

by using a sequence of deformation magnitudes as input data. The overall change in the orientation of the intelligent sensor could be measured from a sequence of detectable steps. Each step is represented as a temporal spatial state of the sensor. Using the state representation, the research question is to uncover the current state of the system, in terms of sensor rotation R_t^p , given a sequence of partially observed states of the environment computed from speckle patterns $O_{1:t}$. The main motivation for using LSTM is to track the previous states of the system and use it for estimation of the current rotation angle. Here, the LSTM model act as a function K that maps deformation to the sensor's rotation::

$$R_t^p = K(O_{1:t},\ R_0^p) \tag{4.6}$$

where R_0^p is the previous or initial state of the system. Given such a mapping function, one can iterate over series of deformation parameters as tip of a fiber deflects, and estimate the sensor's heading angles.

The architecture of the LSTM model is represented in Fig. 4.15. This model has one input layer, three LSTM layers to extract temporal information, and one dense layer to generate regressional output. In out experience, this architecture is the simplest architecture capable of providing reliable and stable results. The input to the network is a sequence of deformation magnitudes. Each input sequence has 15 data points. The first, the second and the third LSTM layers have 8, 5 and 3 neurons, respectively, and are followed by RELU activation function. Also, a dropout layer was utilized to prevent overfitting. Similar to the previous studies, the Mean Square Error (MSE) loss function was used to train the model. To construct the train and test datasets, we used the collected pendulum local heading angle to represent the intelligent sensor's heading angle , as well as the acceleration data to represents the deformation of the fiber. After normalizing the data, the acceleration data was grouped into sequences of 15 samples, and was associated with one rotation sample. Then a train set, and a test set was created by splitting the dataset into 80/20 train/test ratio. Also, 20% percent of the training test was used as the validation set. The total number of samples in the train set, validation set, and test set were $66,628\times\ 15$, $15,262\times\ 15$ and $19,077\times\ 15$ respectively. The LSTM model was trained to learns the mapping between the sequences of deformation magnitudes and the corresponding rotation of the fiber's base using the training set. Once the model was trained, its performance was evaluated by using unseen deformation sequences from the test set.

4.3.1 Experimental Results

The goal of this experiment was to estimate the orientation angle of the intelligent sensor from its fiber optic tip deformation. We trained a LSTM model as a regressor to find the best fit between the fiber's deformation magnitudes and the sensor's orientation. The model's input and the target variable were acceleration and pendulum deviation angle from its resting position, respectively. The mean square error loss function and the Adam optimizer [82] with an initial learning rate of 0.0001 were utilized to train the model. The model was trained for 80 epochs using the batch size of 50 samples. After the training, the performance of the model was evaluated by

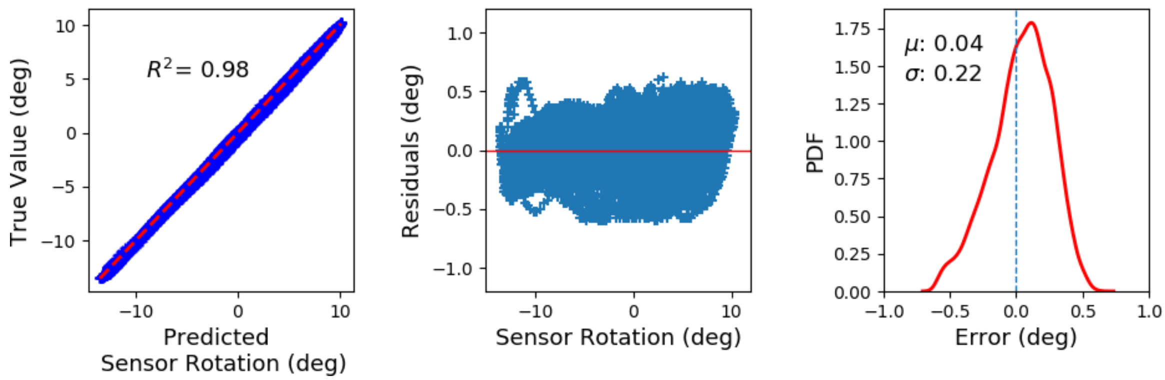

Figure 4.16: (Left Panel) Scatter plots of the actual vs predicted values showing the deviation of the predictions from the ground truth. We can see that all the points are be close to the diagonal line, indicating an effective model. (Middle Panel) The residuals vs. prediction plot demonstrating errors have equal valiance, and clustered around zero. Also, the distribution of the errors is normal, as shown in the right panel.

comparing the model's estimation of the pendulum deviation angle with the actual values using R-squared metrics as presented in equation 4.3.

Fig. 4.16 provides a visualization of how well the LSTM fits the test data. The plot on the far left indicates a strong correlation between the model's prediction of the pendulum deviation angles and the actual values ($R^2 = 0.98$). The residual plot, Fig. 4.16 (middle panel), provides a better insight into the model's performance. We can see that the magnitude of errors are within the ±1 degrees of the actual values. Although the majority of the residuals are distrusted randomly, there are a few non-linear patterns where the deviation angle is toward the extreme −10 degree. The existence of white noise due to the vibration of the pendulum apparatus combined with the high sensitivity of the reference accelerometer are possible sources of this non-linear patterns. The overall distribution of the residuals suggest that the predicted values are slightly biased. This is confirmed by the distribution plot of the errors, presented in the Fig. 4.16 (left panel). We can see that the error distribution is normal, but it is not centered on zero (0.04 ∓ 0.22 deg). Fig. 4.17 presents the probability density function of the predicted orientation angle of the intelligent sensor. We can see

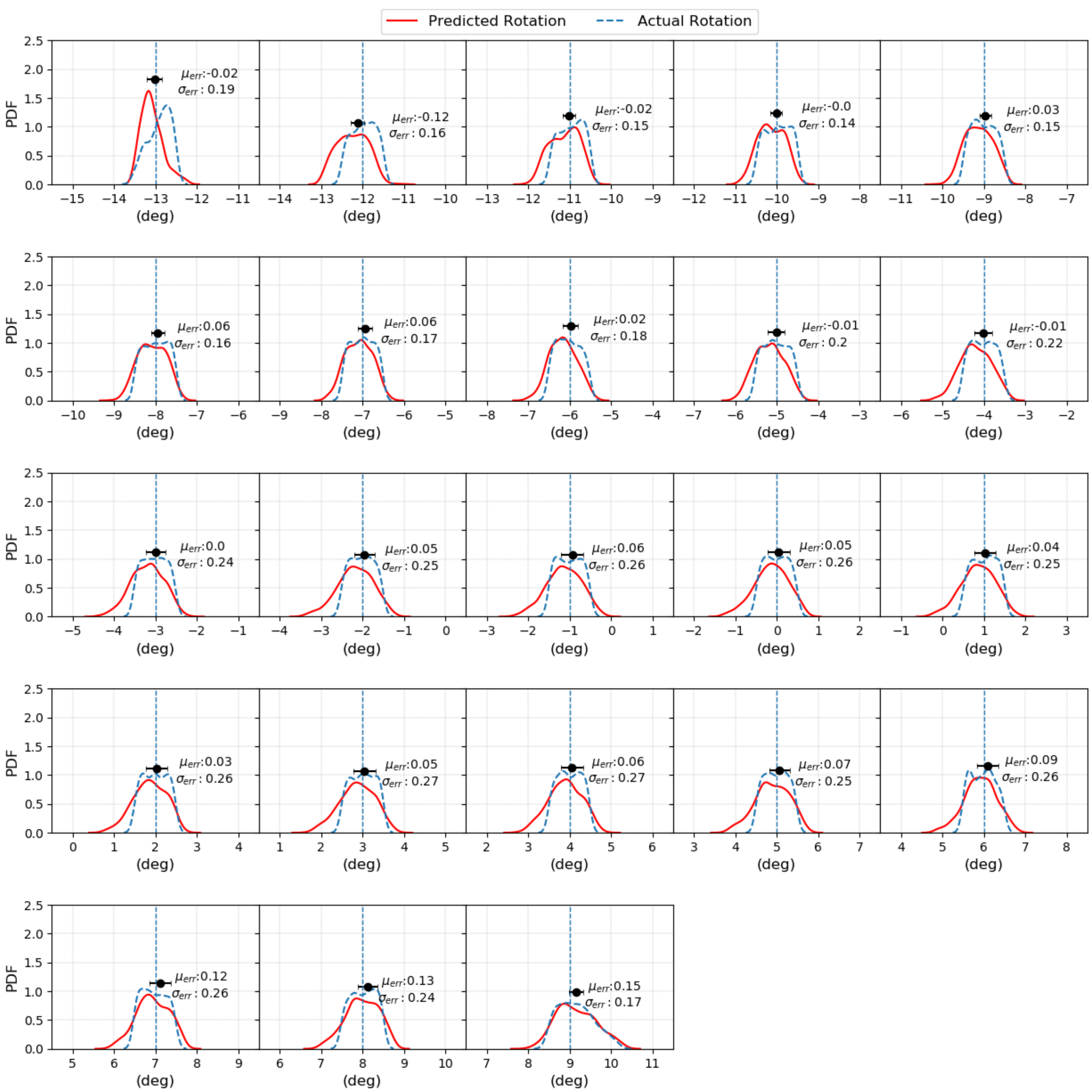

Figure 4.17: Probability Density Function of the predicted orientation angle of the intelligent sensor.

that for the entire range of the pendulum deviation, the distributions of the predicted angles are identical with the distributions of the actual deviation values. Overall, these results provides the proof-of-concept that LSTM models can be exploited to estimate the rotation of the intelligent sensor from the deformation parameters. In the next chapter, we use the results of these studies to track the intelligent sensor's position.

CHAPTER 5: THE INTELLIGENT SENSOR

In chapter 4.1 and 4.2, we demonstrated that specklegram variations contains information for measuring the deformation parameters of a multimode fiber. Also, in chapter 4.3, we provided insights into the physical behavior of the sensor and demonstrated that an LSTM model is capable of estimating the sensor's deviation from its central axis from the deformation parameters of its fiber tip. In this chapter, we utilize the results of the previous chapters to develop a computational pipeline for the intelligent sensor so that it could generate a set of coordinates at an appropriate sampling rate. These coordinates as a set represent the sensor's trajectory.

It is important to note that we used acceleration as an indirect measure of the multimode fiber's deformation. That means the sensor's configuration can be considered as a fiber accelerometer [79]. Theoretically, it is possible to estimate displacement parameters from acceleration assuming the initial state of a system is known. After all, there is extensive research on the application of accelerometer for trajectory estimation. However, in practice, this naive approach is prone to inevitable drifting errors. This is because to obtain position $p(t)$ from acceleration a, the accelerometer readouts are integrated twice:

$$p(t) = \int v dt = \iint a dt \tag{5.1}$$

Moreover, the acceleration magnitude must be adjusted for the gravity factor by using the estimation of orientation. Thus, accelerometers are fused with additional sensors such as a gyroscope or magnetometers. These solutions are far from perfect because all errors in measurement estimation will propagate in time affecting the upcoming calculations. Aside from this, the fusion of accelerometer and other sensors does not suit the in vivo nature of IVUS applications.

5.1 Computational Pipeline

As the sensor travels in space, it captures a set of speckle patterns such as $I_{0:n} = \{I_0, ..., I_{K-n}, I_K\}$ where I_K denotes the speckle image captured at time instance K. Let $W_{0:K} = \{W_{1,0}, ..., W_{K,K-n}\}$ denote the motion of the sensor in the world coordinate system (WCS), where W_0 being the sensor's initial position at time $t = 0$, equal to I or any arbitrarily known value. Also, assume the sensor's displacement Δl_K along its central axis during t_{k-n} is a known value. Our objective is to estimate the sensor's local transformation P_K, and to recover its overall trajectory $W_{0:K}$. The motion model of the sensor is explicitly explained in 3.1.1. In summary, they are as follows:

$$W_K = W_{K-n}.P_K \tag{5.2}$$

$$P_K = \begin{pmatrix} R_{K,K-n} & T_{K,K-n} \\ 0 & 1 \end{pmatrix} \tag{5.3}$$

$$T_{K,K-n} = \frac{\Delta l_K}{\theta} \begin{pmatrix} C\alpha(1 - C\theta) & S\alpha(1 - C\theta) & S\theta \end{pmatrix} \tag{5.4}$$

$$R_{K,K-n} = \begin{pmatrix} C^2\alpha C\theta + S^2\alpha & C\alpha S\alpha C\theta - C\alpha S\alpha & C\alpha S\theta \\ C\alpha S\alpha C\theta - C\alpha S\alpha & S^2\alpha C\theta + C^2\alpha & S\alpha S\theta \\ -C\alpha S\theta & -S\alpha S\theta & C\theta \end{pmatrix} \tag{5.5}$$

where, $C\alpha = \cos\alpha$, $C\theta = \cos\theta$, $S\alpha = \sin\alpha$, and $S\theta = \sin\theta$. Also, $\theta \geq 0$ is the bending angle of the sensor, and $\alpha \in [0, 2\pi]$ represents the direction of bending during $t_{k-n} \to t_k$.

Algorithm 1: Computational Pipeline of the Intelligent Sensor

Require: CNN_θ, CNN_α, $LSTM_\theta$
Input: Sets of specklegram Images $I_{0\to k}$, Axial displacements $\Delta l_{0\to k}$
Result: Trajectory $W_{0\to k}$
Initialization $W_0 = I$, $i = 1$, $winSize = 15$
if $k < winSize$ **then** Exit;
while $i \leq k - winSize$ **do**
  Generate a batch of images: $[I_{i\to i+winSize}]$
  Get CNN_α predictions of bending directions $[\alpha_{winSize}]$ from $[I_{i\to i+winSize}]$
  Set α_{deg} to the most frequent value in $[\alpha_{winSize}]$
  Get CNN_θ predictions of bending angles $[\theta_{winSize}]$ from $[I_{i\to i+winSize}]$
  Get $LSTM_\theta$ predictions of sensor's rotation θ_{deg} from $[\theta_{winSize}]$
  Scale and convert θ_{deg} and α_{deg} to radians: θ_{rad}, α_{rad}
  $\theta_{rad} = ABS(\theta_{rad})$
  if $\theta_{rad} == 0$ **then**
    $T_i = [0, 0, \Delta l]$
  else
    Estimate T_i from $\Delta l_i, \theta_{rad}$, α_{rad} using Eq. 5.4
  end
  Estimate R_i from θ_{rad}, α_{rad} using Eq. 5.5
  $P_i = \begin{pmatrix} R_i & T_i \\ o & 1 \end{pmatrix}$
  $W_i = W_{i-1}.P_i$
end

Using these equations, the algorithmic pipeline for trajectory estimation of the sensor is represented in Alg. 1. Here, CNN_θ and CNN_α denote two trained deep learning models for estimation of the bending angle θ, and direction bending α, respectively. Also, $LSTM_\theta$ is the trained LSTM model, which maps the sensor's tip deformation to its local rotation. The operation of the trajectory estimation pipeline is as follows.

As the sensor travels, speckle images are captured by the camera, and stored on a storage drive. A batch generator unit reads a pre-defined $winSize$ sequence of speckle images from the storage, and crops them from 450×450 pixels to 420×420 pixels in order to reduce the dark region surrounding the specklegrams. The batch generator unit also down-samples the images to 300×300 pixels, converts them to gray-scale images, applies a Gaussian blur filter, and normalized the images. At each iteration, the output of the batch generator unit is a batch of specklegram images $[I_{i\to i+winSize}]$, ready to be processed with the CNN_θ and CNN_α models for the extraction of the deformation parameters. For each image $I_K \in [I_{i \to i+winSize}]$, the CNN_α estimates the direction of deformation. After all images were processed, the CNN_α unit returns a prediction array $[\alpha_{winSize}]$ with the size $winSize \times 1$. Then, α_{deg} is set to the most frequent value of this array.

Similarly, CNN reads the $[I_{i \to i+winSize}]$ batch in the i_{th} iteration and returns an array of bending angles $[\theta_{winSize}]$, which is directly fed to the $LSTM_\theta$ to estimate the sensor's rotation based on the deformation parameters. The output of the $LSTM_\theta$ is the a scalar θ_{deg}, which represents the sensor's deviation from its central axis. Both α_{deg} and θ_{deg} are scaled back using the scaling parameters of the system, which were obtained during the data collection process, and the training data. At this point, the bending direction is within the proper range of $\alpha_{rad} \in [0, 2\pi]$. However, the deformation magnitute corresponds to the entire raneg of deformation. This is because the $LSTM_\theta$ model was trained to calculate the sensor's rotation for the overall axis of deformation parameters. Therefore, the final step before calculating the sensor's trajectory is to set θ_{rad} equal to its absolute value: $\theta_{rad} = ABS(\theta_{rad}) \geq 0$. Finally, the sensor's overall trajectory is calculated from the equations 5.2 to 5.5.

To evaluate the trajectory estimation, the motion equations were used to derive the trajectory of the pendulum system from the speckle patterns. For this means, we required an ordered sequence of speckle samples representing the pendulum oscillation. We also needed to ensure than the deep learning models have not seen any of the samples before. To satisfy both requirements, first, we used the entire the previously collected data ($82,250$ samples) to re-trained the deep learning models. Then, we collected a new test set with 8,054 samples using the pendulum system. The performance of the trajectory estimation algorithm was evaluated using the speckle patterns from the test set. The details of the validation process have been described in detail in section 3.1.2. In summary, validation steps are as follows. 1. Construct-

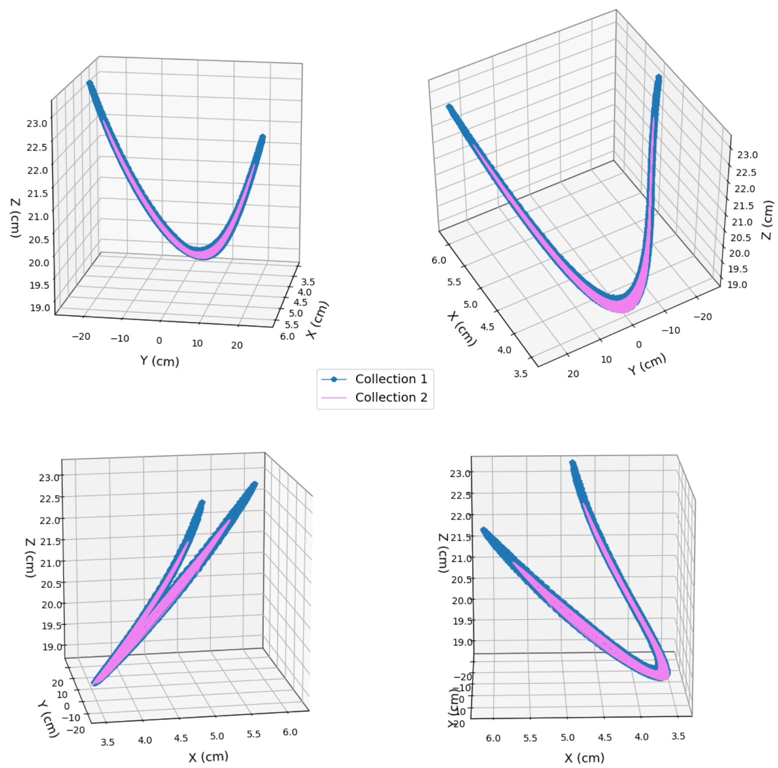

Figure 5.1: 3D Visualization of the Pendulum Trajectory as captured by the Reference Tracker.

ing a reference distribution as a baseline. 2. Evaluating the motion equations by applying the reference sensor readouts and comparing the results with the baseline. 3. Evaluating the intelligent sensor estimated trajectory with the baseline.

5.2 The Reference Distribution

The trajectory of the pendulum apparatus was used to construct the baseline reference distribution. Assuming the pendulum parameters and its starting release point remain constant, it goes through similar harmonic motion. To construct the evaluation set, two collections of the pendulum motion were recorded. The data collection process was similar to the steps explained at chapter 3.2.1. Also, a periodic force was applied to the pendulum to maintain its motion. Fig. 5.1 provides a visualization of the pendulum trajectory as it was recorded with the reference position tracker. After pre-processing and removing the outliers, each collection contained 8022 sam-

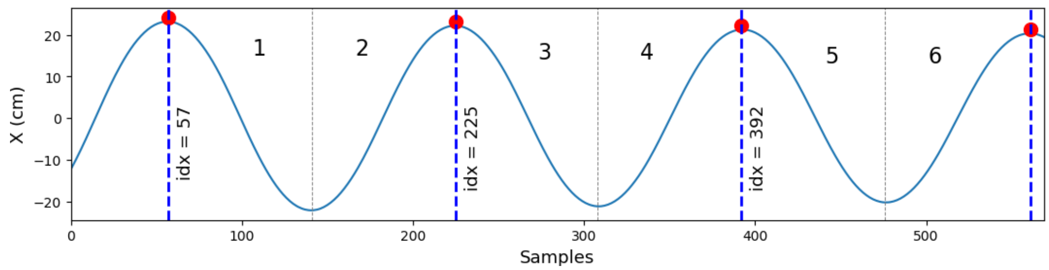

Figure 5.2: To extract observations, the starting points of each pendulum cycle were identified, shown by the red markers. The interval between two consecutive picks represents two observations.

ples corresponding to 70 seconds. To extract observations, signal processing was used to identify the picks of the motion signal, see Fig. 5.2. These picks represent the starting points of one complete cycle. Within each half cycle, the back-and-forth displacement of the pendulum are approximately equal in length. Therefor, the pendulum's motion within each interval was counted as two observations. Also, random samples of 2, 3, and 4 consecutive cycles were selected from each collections, and were added to the observations to account for the accumulation of errors. We made sure the corresponding randomly-selected observations between collections have identical starting time-index and length. Finally, through the steps explained in 3.1.2, the reference distance distribution and the DDTW distribution were constructed using 2306 observations, shown in Fig. 5.3.

These two distributions provides the baseline parameters to analyse and evalu-

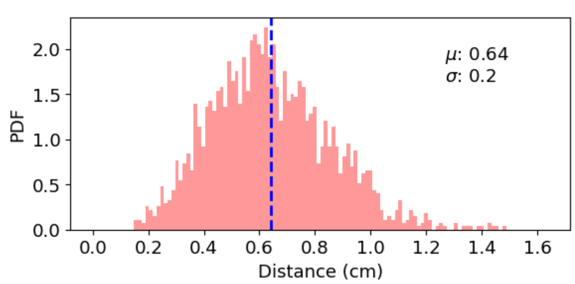

(a) The reference distance distribution

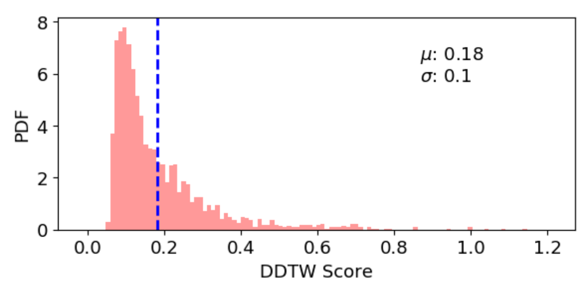

(b) The reference DDTW distribution

Figure 5.3: These two distributions provide the baseline parameters to evaluate the intelligent sensor.

ate the intelligent sensor. Ideally, the measurements of the reference tracking sensor should be identical, and thus, align together. However, the average distance between the observations is $0.64 \pm 0.4\ cm$. Also, the average DDTW distance between observations is 0.18 ± 0.1. Note that the DDTW distance is a non-metric unit-less similarity measure [76]. The possible sources of the difference between observations are the reference tracking sensor estimation error, the pendulum vibrations while collecting data, small differences in the starting release position of the pendulum, and the inconsistency in timing of the applied force.

5.3 Evaluation of the Motion Model

The next step in the validation process was to evaluate the motion model represented by equations (5.2 to 5.5). Our goal was to understand the influence of underlying simplification assumptions of the model on the estimated trajectory. Through an iterative process, the pendulum's end-point displacement parameters were applied to the motion model to obtain the trajectory. The motion model takes three parameters: Δl, θ and α. At each time instant i, Δl was calculated by comparing the reference sensor's read-outs between time t and $t-1$. Also, θ and α were calculated from the the pendulum's end-point position (P_x, P_y, P_z) using the following inverse kinematic equations [72, 73, 74, 75]:

$$\theta_i = Arctan(\frac{P_y}{P_x}) \tag{5.6}$$

$$\alpha_i = Arccos(\frac{1-K}{1+K}) \tag{5.7}$$

$$K = \frac{P_y^2}{P_z^2 \sin^2_{\theta_i}} \tag{5.8}$$

The initial results are provided in the middle panel of the Fig. 5.4. The Z and Y axes are the vertical and horizontal components of the pendulum's motion. The X-axis represents the deviation of the pendulum from the YZ plane. The shapes of the

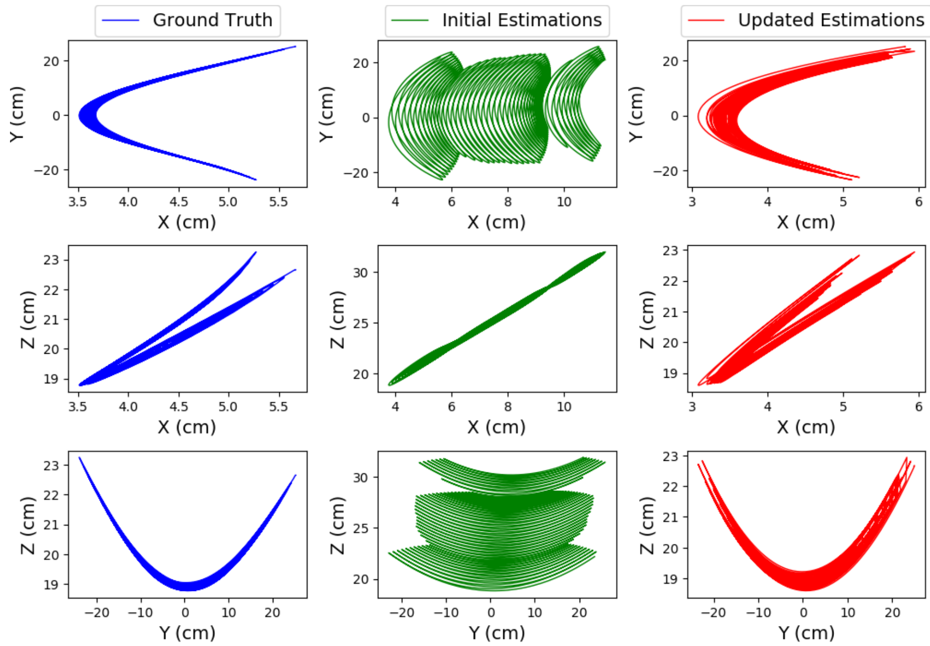

Figure 5.4: The first column shows the pendulum trajectory as it was recorded by the reference tracker. In the middle panel we can see the motion model estimations are subjected to accumulation of errors. (Right Panel) Error propagation is significantly reduced after applying a periodic corrections.

estimated trajectories follows a similar trend to its true value within one oscillation (half cycle). However, the estimations were affected by accumulative errors in time. This was an expected outcome. Error accumulation is an inevitable component of trajectory estimation for problems, in which, an external point of reference is not available. This type of error has two sources: the error in the read-outs of the reference tracker, and the accumulation of the round-off-error when incrementing the trajectory position in time. The round-off error is a well-known consequence of motion estimation by multiplication of a sequence of transformation matrices without applying any method to correct errors [89]. To limit the propagation of errors, and yet being able to study their influence, the model estimations were corrected periodically by their true values at the end of every two cycles. The results are shown in Fig. 5.4, right column. Although there still exists some error in the estimation of the motion models, the influence of error propagation is limited. The trend and distributions of

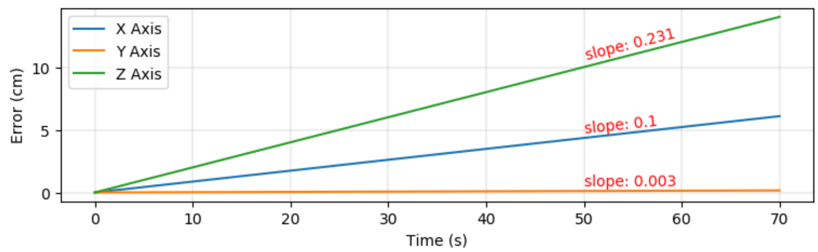

(a) Error propagation rate for each Axis of motion

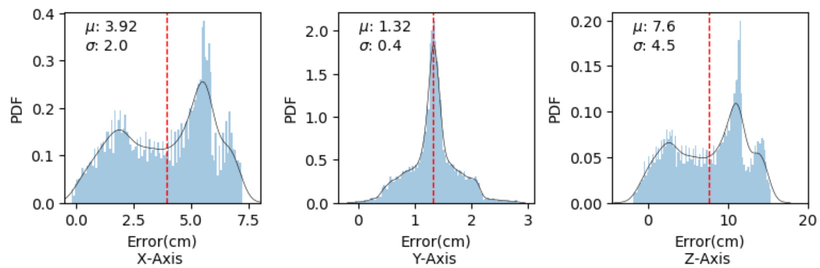

(b) Distribution of Errors prior to applying the corrections.

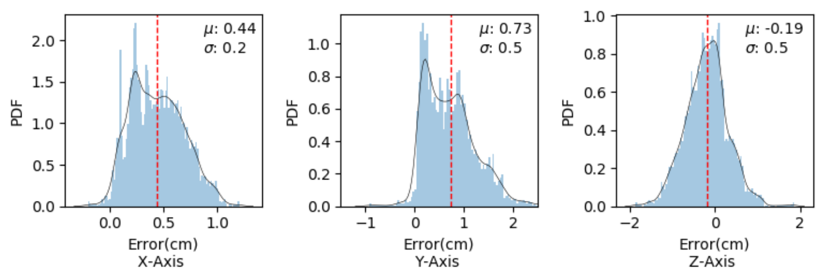

(c) Distribution of Errors after applying the corrections

Figure 5.5: The trend and distributions of accumulated errors for each axis of motion before and after applying the corrections.

accumulated errors for each axis of motion before and after applying the corrections are presented in Fig. 5.5. These results suggest that errors are accumulated linearly in time.

Fig. 5.6 provides a comprehensive comparison between the motion model estimated trajectory of the pendulum with its true values for two consecutive observations, or one pendulum cycle. The largest deviations between the ground truth and the estimated values for X, Y, and Z directions are 1.1 cm, 2.98 cm and 2.0 cm, respectively, shown in the third row. The distributions of the errors are provided in the last row. The average estimation errors in the X, Y, and Z axes are 0.400 ± 0.4 cm, 1.54 ± 0.8 cm, and -0.51 ± 0.7 cm, respectively. In X-axis and Y-axis, the largest deviation between

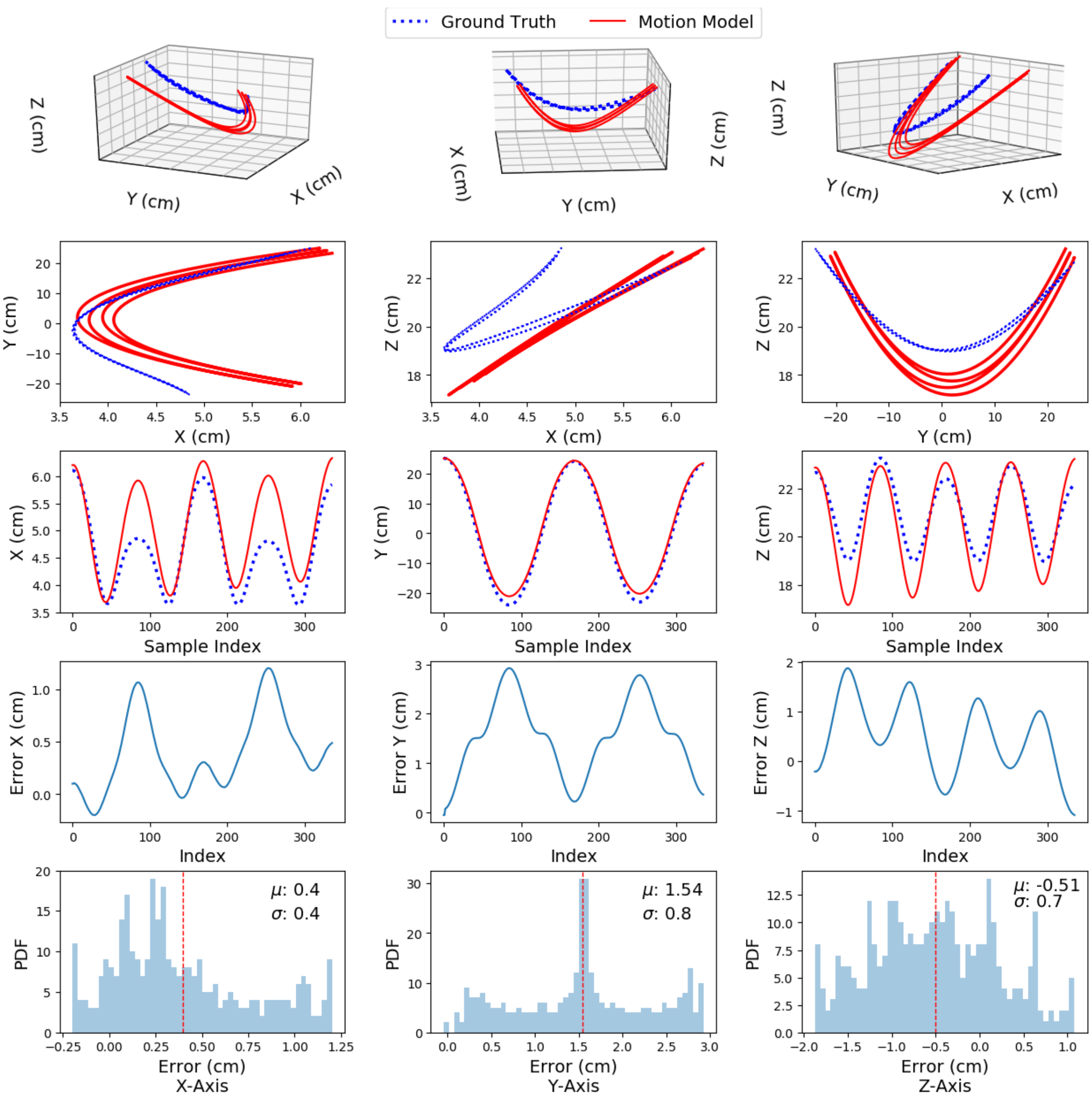

Figure 5.6: The first and the second rows provide the 3D and 2D views of the results. The degree to which these two curves are aligned can be seen in the third row. Errors and their distributions are provided in the last two rows.

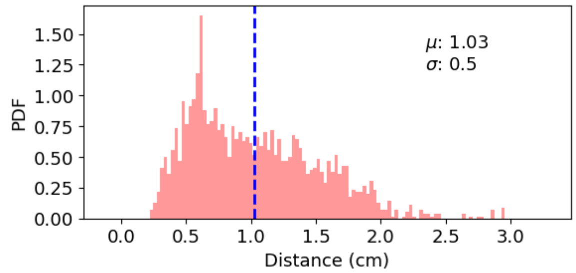

(a) Motion model distance distribution

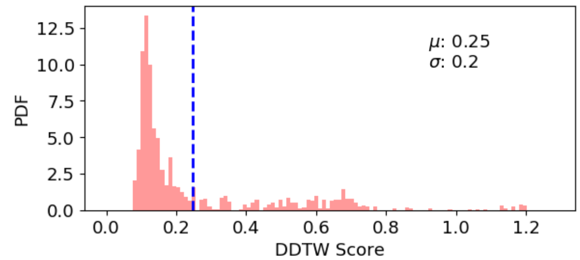

(b) Motion model DDTW distribution

Figure 5.7: These two distributions represent a summary of the motion model performance for 2,036 observations.

the two trajectories corresponds to the ending point of the first oscillation, i.e., half cycle, where the pendulum stops momentarily and restarts its motion in the opposite direction. The most possible source of this deviation is the weight of the pendulum apparatus, which produces a periodic torque vibration.

Fig. 5.7 shows the distributions of DDTW score and the average distance between the motion model estimations and the true values for all observations. The average distance between the estimations and the ground truth is a $1.03 \pm 0.5\ cm$. Also, the average DDTW score is 0.25 ± 0.2 . In the next section, the reference distributions as well as these two distributions will be used to evaluate the intelligent sensor.

5.4 Evaluation of the Intelligent Sensor

To evaluate the intelligent sensor, the sequences of speckle patterns from the test collection were used to derive the pendulum's motion. The Speckle patterns were pre-processed as was explained in the chapter 3.2.3. Then, the trajectory of the pendulum was detected from the Alg. 1. Similar to the previous section, estimations were periodically updated (every two cycles) to limit the propagation of errors. Fig. 5.8 shows the intelligent sensor's estimation before and after applying the periodic correction. These estimations correspond to the entire test collection, i.e. 7941 samples, 2036 observations. The Y and Z axes are the vertical and horizontal components of the pendulum's motion. The X-axis represents the deviation of the pendulum from

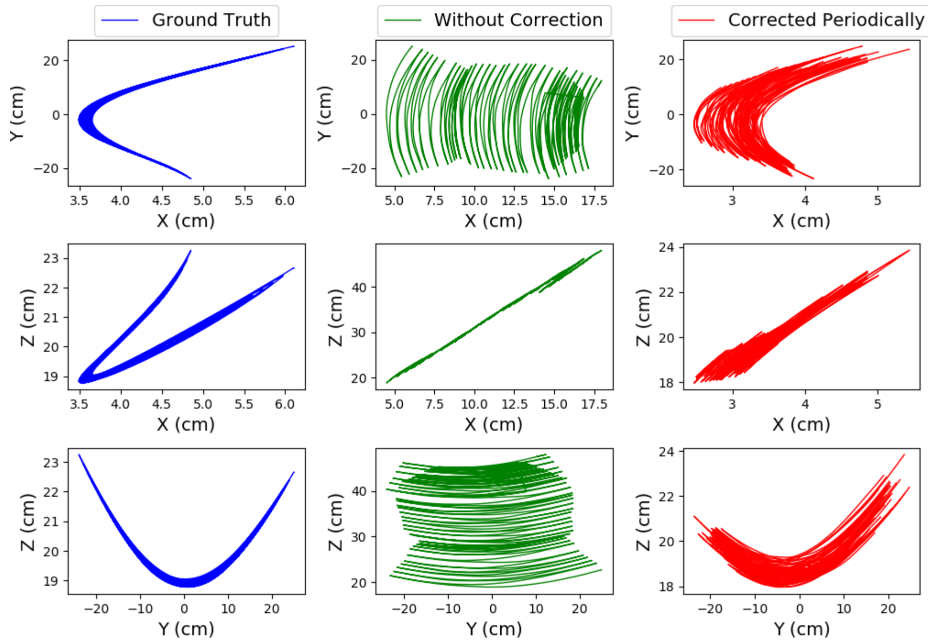

Figure 5.8: The first column shows the pendulum trajectory as it was recorded by the reference tracker. In the middle panel we can see that the estimations intelligent sensor are subjected to accumulation of errors. (Right Panel) Error propagation is significantly reduced after applying a periodic corrections.

the YZ plane. Comparing the XZ and YZ planes of the estimates trajectories with the ground truth values reveals that the highest error propagation rate is in the Z direction, i.e. vertical component of the motion. After applying the corrections, the estimates trajectory in the XZ view has the lowest similarity to the reference trajectory. These initial observations suggest that the intelligent sensor underestimates the pendulum's deviation from the YZ plane. Thus, the Z component of motion is overestimated.

Table 5.1: Comparison of Estimation Errors

	Axis	Motion Model	Intelligent Sensor
Without Correction	X	$3.92 \pm 2.0\ cm$	$13.74 \pm 6.9\ cm$
	Y	$1.32 \pm 0.4\ cm$	$4.04 \pm 2.6\ cm$
	Z	$7.6 \pm 4.5\ cm$	$16.39 \pm 8.2\ cm$
Periodically Corrected	X	$0.44 \pm 0.2\ cm$	$0.33 \pm 0.6\ cm$
	Y	$0.73 \pm 0.5\ cm$	$0.08 \pm 0.5\ cm$
	Z	$0.19 \pm 0.5\ cm$	$0.18 \pm 0.8\ cm$

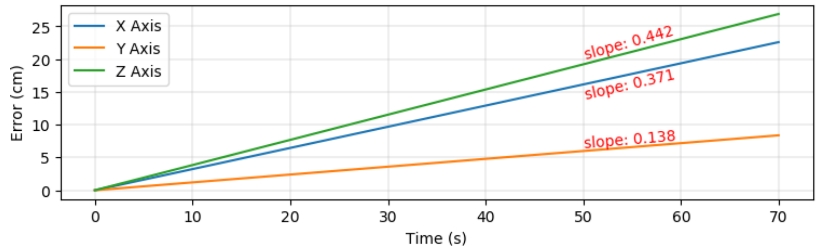

(a) Error propagation rate for each Axis of motion

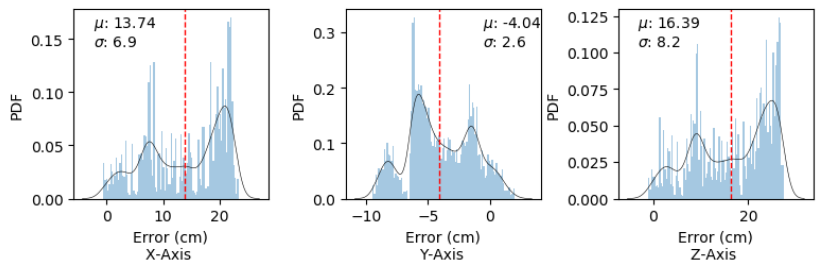

(b) Distribution of Errors prior to applying the corrections.

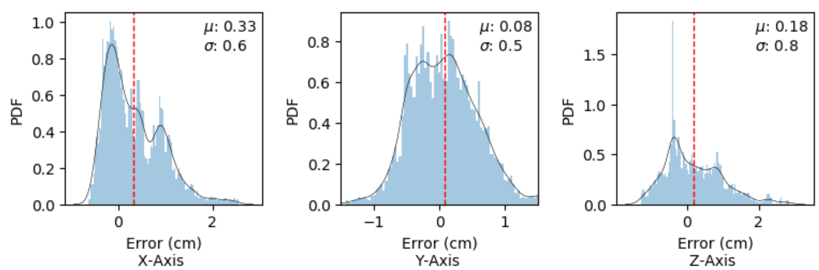

(c) Distribution of Errors after applying the corrections

Figure 5.9: The trend and distributions of accumulated errors for each axis of motion before and after applying the corrections.

The trends and distribution of the errors before and after applying the correction are provided in Fig. 5.9. In comparison to the motion model, i.e. Fig. 5.5, the error propagation rate of the intelligent sensor has increased from 0.1 cm/s to 0.371 cm/s in the X direction, from 0.003 cm/s to 0.138 cm/sin the Y direction, and from 0.231 cm/s to 0.442 cm/s in the Z direction. Table. 5.1 provides a comprehensive comparison between the motion model and the intelligent sensor estimations before and after applying the periodic correction. Prior to applying the corrections, the average error in the X, Y, and Z-axis of displacement are $13.74 \pm 6.9\ cm, 4.04 \pm 2.6\ cm$, and $16.39 \pm 8.2\ cm$, respectively. After applying the correction, the errors were reduced to $0.33 \pm 0.6\ cm, 0.83 \pm 0.5\ cm$, and $0.18 \pm 0.8\ cm$. These results suggest that the intelligent sensor provides an approximate estimation of the pendulum trajectory. However, without having an error correction method, the errors accumulate rather quickly.

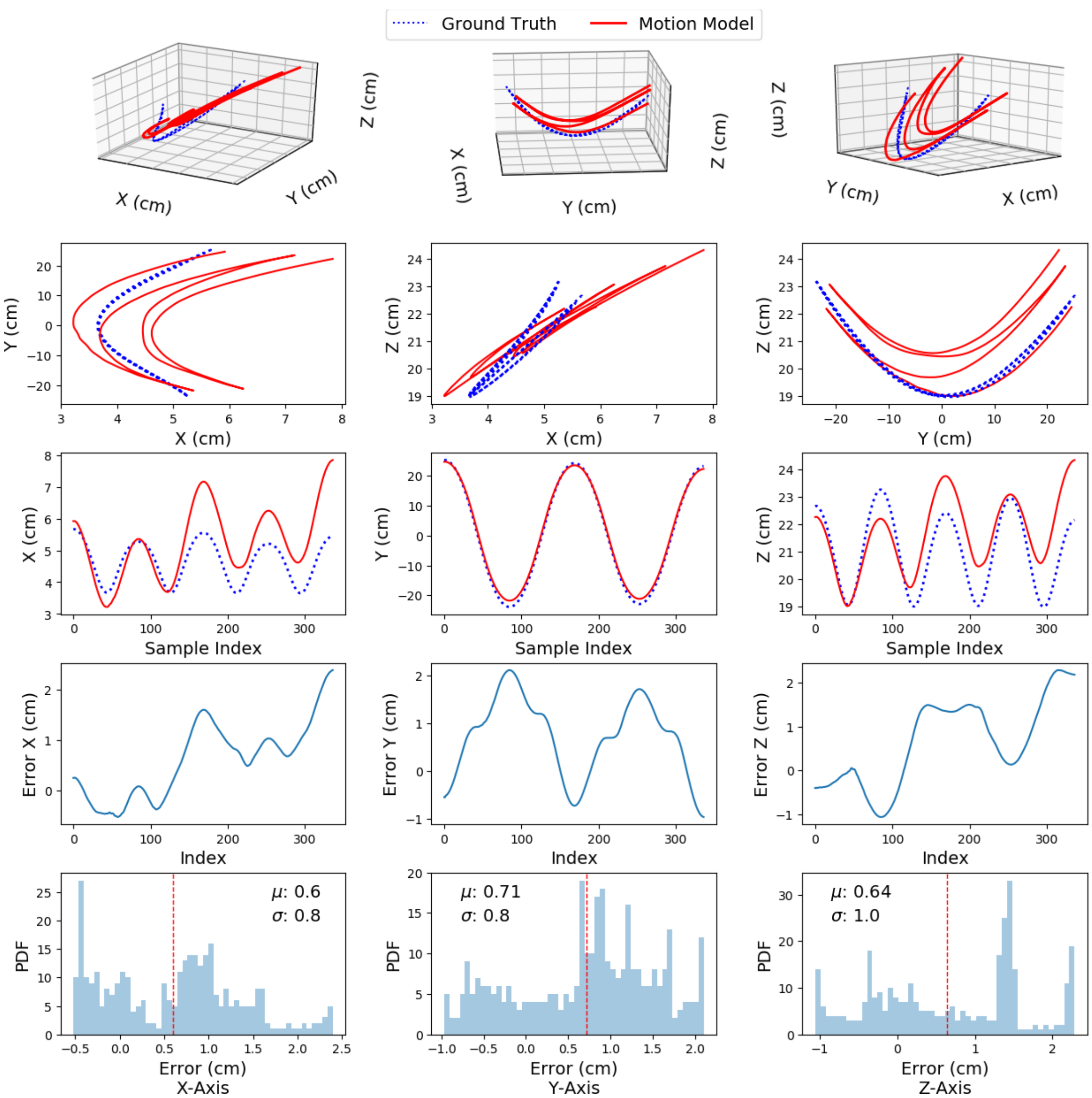

Figure 5.10: The first and the second rows provide the 3D and 2D views of the results. The degree to which these two curves are aligned can be seen in the third row. Errors and their distributions are provided in the last two rows.

Fig. 5.10 presents the intelligent sensor estimated motion trajectory of the pendulum in one cycle, i.e. two observations. The average error in the X, Y, and Z-axis of displacement are $0.64 \pm 0.8\ cm, 0.71 \pm 0.8\ cm$, and $0.64 \pm 1.00\ cm$, respectively. The divergences between the shape of the estimated trajectories and the references are

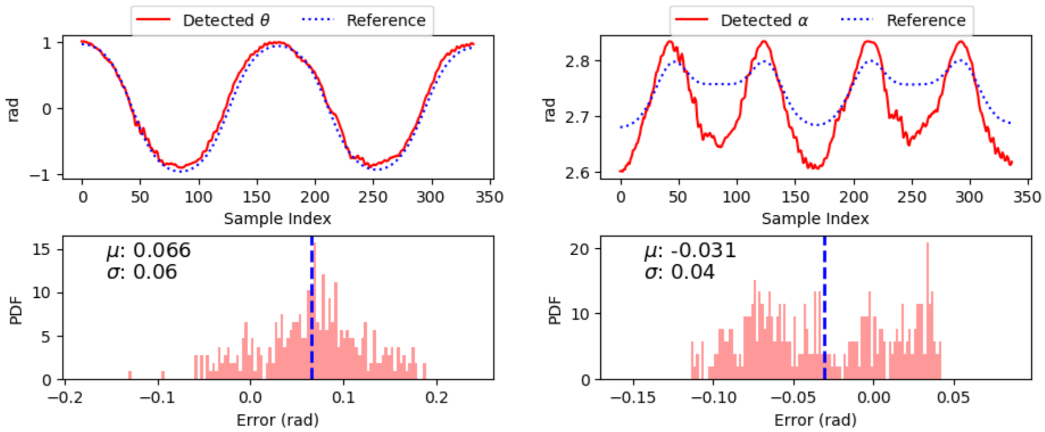

Figure 5.11: Comparison between the estimated orientations of the sensing transducer and their true values.

shown by XY, XZ, and YZ planes. A comparison between the Fig. 5.10 and Fig 5.6 revels that the divergence between the estimations and the true values follow a similar pattern, i.e. errors are larger when the pendulum stops and changes its displacement direction. To provide more insights, a comparison between the estimated orientations of the sensing transducer, i.e. α and θ, and their reference values are provided in Fig. 5.11. The average error in the estimated sensor deviation from its central axis, i.e. θ was 0.07 ± 0.1 rad. Also, the average estimation error of the direction of deviation was -0.03 ± 0.001 rad. The small magnitude of these errors indicates speckle analysis and the deep learning pipeline provides an accurate estimation of orientation of the intelligent sensor.

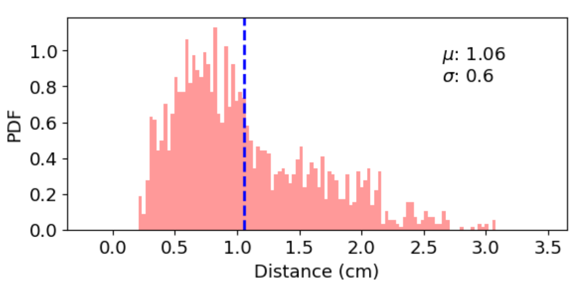

(a) Distance distribution

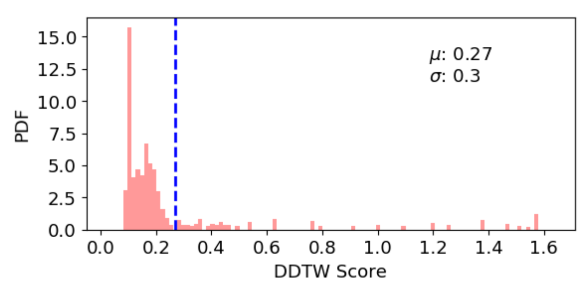

(b) DDTW distribution

Figure 5.12: These two distributions represent a summary of the Intelligent Sensor performance for 2,036 observations.

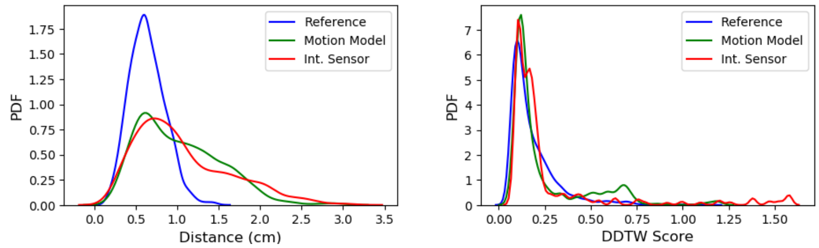

(a) Probability density functions of the distributions

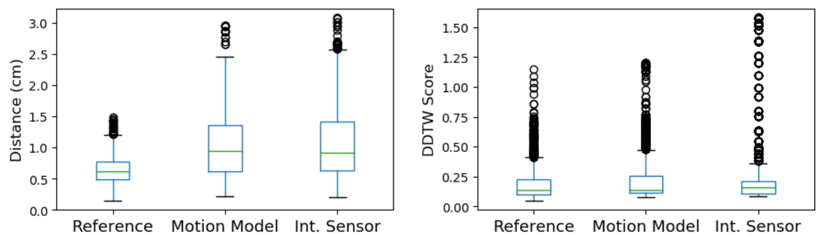

(b) Box-plot visualization of the distributions

Figure 5.13: Overview of the distance and DDTW distributions of the ground truth, motion model, and the intelligent sensor.

Fig. 5.12 shows the distributions of DDTW score and the average distance between the intelligent sensor estimations and the true values for all observations. The average DDTW score between the intelligent sensor results and the reference trajectory is 1.06 ± 0.6. The average distance between the intelligent sensor's estimations and the ground truth is a 0.27 ± 0.3 .

Fig. 5.13 provides a comprehensive visual overview of the distance and DDTW distributions of the ground truth, motion model, and the intelligent sensor. These distributions were compared using t-test, Kolmogorov-Smirnov (K-S) test, and Mann-Whitney U-test. The t-test analysis between the distance distribution of the reference and motion model shows these distributions are significantly different ($t = -32.473$, $p < 2.2E-16$). This is also confirmed with the Mann-Whitney U-test($p < 2.2e - 16$), and the K-S test ($D = 0.414$, $p < 2.2E-16$). The t-test analysis between distance distribution of the the reference and the intelligent sensor shows they are significantly different ($t = -31.423$, $p < 2.2E-16$), which was confirmed by the Mann-Whitney U-test($p < 2.2E-16$), and the K-S test ($D = 0.401$, $p < 2.2E-16$).

The comparison between the distance distribution of the intelligent sensor and motion model did not yield a consistent results. According to the t-test ($t = -2.0163$, $p = 0.043$) and K-S test ($D = 0.062$, $p = 0.000$) these distributions are significantly different at 95% confidence interval. However, the Mann-Whitney U-test failed to reject the null hypothesis ($p = 0.5495$).

The results of comparing the DDTW distributions are as follows. The t-test analysis between the DDTW distribution of the motion model and the reference shows these distributions were not significantly different ($t = -11.349$, $p < 2.2E-16$). This was also confirmed using the Mann-Whitney U-test ($p < 2.2E-16$) and the K-S test ($D = 0.191$, $p < 2.2E-16$). The DDTW distribution of the intelligent sensor were statistically different from the reference DDTW distribution using t-test ($t = -11.035$, $p < 2.2E-16$), and the Mann-Whitney U-test ($p < 1.9E-8$), and the K-S test ($D = 0.218$, $p < 2.2E-16$). Finally, The DDTW distribution of the intelligent sensor were statistically different from the motion model DDTW distribution using t-test ($t = -2.385$, $p = 0.02$), and the K-S test ($D = 0.128$, $p < 2.2E-16$). However, the Mann-Whitney U-test failed to reject the null hypothesis ($p = 0.275$).

To provide more insights, the empirical cumulative distribution function (ECDF) of the all distributions are provided in Fig. 5.14. While the distribution of the motion model and the intelligent sensor estimations are similar to each other, they are significantly different from the reference distribution. Similarly, we can see that the DDTW distribution of the intelligent senor and the motion model are more similar to each other and significantly different from the reference distribution. The difference between the reference and motion model estimations – which were made from the reference values– suggests this motion model is the source of the intelligent sensor's estimation errors. Additionally, error accumulation is the another source of the error in the estimations. It is important to note that the intelligent sensor, and the motion model were not calibrated. Therefore, we conclude these results provide a proof-of-

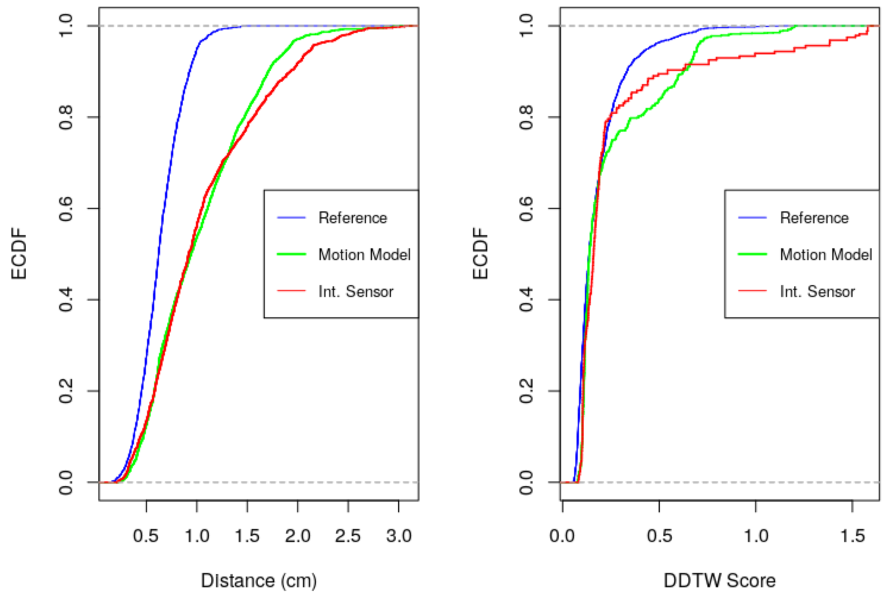

Figure 5.14: Empirical cumulative distribution function (ECDF) of the ground truth, motion model estimations, and the intelligent sensor estimations.

concept that utilizing speckle patterns for motion estimation is a feasible approach, and the estimations of the intelligent sensor are similar to those of which were made by the motion model from the ground truth values.

CHAPTER 6: DISCUSSION

In this study, we explored the possibility of speckle patterns analysis for tracking motion in the context of cardiovascular research. We utilized a computation pipeline to extract featured from sequences of speckle patterns and to derive motion parameters from those features. In chapter 3 we presented the design, motion model and validation process of an intelligent sensor to track motion. The presented sensor incorporated a multimode fiber optic as a transducer. We also constructed a comprehensive dataset for speckle pattern analysis. Using this dataset, we carried out a set of experiments to investigate the feasibility of our approach.

First, we demonstrated that each state of a deforming fiber optic corresponds to a unique speckle pattern. The state of fiber was defined using two parameters: deformation magnitude, and direction (axis) of deformation. The results of our experiments in chapter 4.1 and 4.2 confirmed that variation in the shape of speckle patterns provides deterministic information for measuring the direction (axis) and the angle of a fiber optic deformation.

Second, through a machine learning approach, we calculated the heading direction of the intelligent sensor from the deformation of its fiber optic transducer. As explained in chapter 4.3, three rounds of simulation studies were performed to observe the fiber's oscillating behavior and also, to check the relationship between the sensor heading direction and the deformation of its sensing fiber tip. The results of these simulations suggested that long-term dependencies between the deformation parameters provide a stable and reliable indication of the intelligent sensor's heading direction. Once this relationship was established, we trained an LSTM model to estimate the intelligent sensor's heading angle from a sequence of deformation parameters. The results of this experiment provided the proof-of-concept that LSTM models can be exploited to estimate the heading direction of the intelligent sensor from the deformation parameters.

At the ends, we utilized the findings of the previous studies to develop a computational pipeline for the intelligent sensor so that it could generate a set of coordinates at an appropriate sampling rate, representing its trajectory, as explained in the chapter 5.1. We tested the intelligent sensor and its computational pipeline on the estimation of a contorlled trajectory. The evaluation process included comparing the intelligent sensor's read-outs to ground truth values, which was obtained from a reference tracker sensor, as well as the estimation of its motion model using the ground truth values. The results indicated that estimations provided by the intelligent sensor and those of which obtained from the motion model have similar distributions.

While the estimation errors do not fit the in vivo application yet, the results provide a proof-of-concept this research is on the right path. There are several factors and limitations to consider:

1. The sensor prototype and data collection setup were bulky instruments subjected to vibrations. Although this system was designed to oscillate in the XY plane, it deviated from its motion plane. This deviation was captured by the intelligent sensor (although underestimated).

2. Another source of error was the miss-alignment between the orientation of the sensor, the reference tracker, and the accelerometer. These factors resulted in the underestimation (or overestimation) of the deformation parameters.

3. Speckle patterns are highly sensitive to the physical status of the multimode fiber. Therefore, this approach may be combined with a signal processing unit to increase the signal to noise ratio.

4. Because the position and orientation of the camera and the multimode fiber

were fixed, the intelligent sensor was not capable of estimating the rotation around its central axis.

5. Speckle patterns are unique for every multimode fiber. Therefore, the training process must be repeated for every fiber. Although applying transfer learning reduces the training time significantly, it does not eliminate it.

The intelligent sensor and the methodology presented here provides an alternative solution for tracking objects. In this regard, this research establishes a foundation for future studies to build upon. Moving forward, future works may include extensions to our approach for further improvements, and utilizing them for other applications. For example:

- In this research, we evaluated the intelligent sensor estimation of the motion of a pendulum. However, this motion does not represent the movement of the IVUS catheter while in vivo. Therefore, the next step of this research will include the assessment of the intelligent sensor in a similar environment, i.e. a tube. Such evaluation will not be possible without the prototyping refinement of the intelligent sensor to fit in such environment. Also, we did not perform sensitivity and range analysis in this study. These aspects have to be further examined to better understand the sensing capabilities and limitations of the intelligent sensor. Finally, future works also include refinements and expanding the intelligent sensor motion model as it directly influences the accuracy of the measurements.

- Many of the problems addressed in this research are also relevant to the other engineering fields. Thus, the results of this study could be applied to broadens the knowledge in other fields. Findings may also shorten the gap between the academic and industry by providing valuable information for researchers who are interested in applying machine learning methods to real-world problems.

REFERENCES

[1] National Center for Health Statistics, "Health, United States, 2016: With Chartbook on Long-term Trends in Health," tech. rep., National Center for Health Statistics., Hyattsville, MD., 2017.

[2] Mozaffarian *et al.*, "Heart disease and stroke statistics-2016 update a report from the American Heart Association," *Circulation*, vol. 133, pp. e38–e48, jan 2016.

[3] Sanidas *et al.*, "Study of atheromatous plaque using intravascular ultrasound.," *Hellenic J. Cardiol.*, vol. 49, no. 6, pp. 415–421, 2008.

[4] S. B. Solomon, T. Dickfeld, and H. Calkins, "Real-time cardiac catheter navigation on three-dimensional CT images," *J. Interv. Card. Electrophysiol.*, vol. 8, no. 1, pp. 27–36, 2003.

[5] A. F. Frangi, W. J. Niessen, and M. A. Viergever, "Three-dimensional modeling for functional analysis of cardiac images: A review," *IEEE Trans. Med. Imaging*, vol. 20, no. 1, pp. 2–25, 2001.

[6] S. Çimen, A. Gooya, M. Grass, and A. F. Frangi, "Reconstruction of coronary arteries from X-ray angiography: A review," 2016.

[7] C. Caucheteur, T. Guo, and J. Albert, "Review of plasmonic fiber optic biochemical sensors: improving the limit of detection," may 2015.

[8] F. Khan, A. Denasi, D. Barrera, J. Madrigal, S. Sales, and S. Misra, "Multi-Core Optical Fibers with Bragg Gratings as Shape Sensor for Flexible Medical Instruments," *IEEE Sensors Journal*, vol. 19, pp. 5878–5884, jul 2019.

[9] C. Shi, S. Giannarou, S. L. Lee, and G. Z. Yang, "Simultaneous catheter and environment modeling for Trans-catheter Aortic Valve Implantation," in *IEEE International Conference on Intelligent Robots and Systems*, pp. 2024–2029, Institute of Electrical and Electronics Engineers Inc., oct 2014.

[10] C. Shi, X. Luo, P. Qi, T. Li, S. Song, Z. Najdovski, T. Fukuda, and H. Ren, "Shape sensing techniques for continuum robots in minimally invasive surgery: A survey," *IEEE Transactions on Biomedical Engineering*, vol. 64, pp. 1665–1678, aug 2017.

[11] M. C. McDaniel, P. Eshtehardi, F. J. Sawaya, J. S. Douglas, and H. Samady, "Contemporary clinical applications of coronary intravascular ultrasound," 2011.

[12] S. B. Kutty, R. W. O. Rahmat, S. Kassim, H. Madzin, and H. Hamdan, "A Review of 3D Reconstruction of Coronary Arteries Based on the Co-registration of IVUS and Coronary Angiogram," in *Proc. - 2014 Int. Conf. Comput. Assist. Syst. Heal. CASH 2014*, pp. 1–5, IEEE, dec 2015.

[13] E. Sanidas and G. Dangas, “Evolution of intravascular assessment of coronary anatomy and physiology: From ultrasound imaging to optical and flow assessment,” sep 2013.

[14] A. Katouzian, E. D. Angelini, S. G. Carlier, J. S. Suri, N. Navab, and A. F. Laine, “A state-of-the-art review on segmentation algorithms in intravascular ultrasound (IVUS) images,” *IEEE Trans. Inf. Technol. Biomed.*, vol. 16, pp. 823–834, sep 2012.

[15] L. Lo Vercio, J. I. Orlando, M. del Fresno, and I. Larrabide, “Assessment of image features for vessel wall segmentation in intravascular ultrasound images,” *Int. J. Comput. Assist. Radiol. Surg.*, vol. 11, pp. 1397–1407, aug 2016.

[16] MultiImagerSurgical.com, *What Is A C-Arm?*, 2013. [Online]. Available: http://www.multiimagersurgical.com/what-is-a-carm. [Accessed: March 10, 2018].

[17] H. Wollschlager, P. Lee, A. Zeiher, U. Solzbach, T. Bonzel, and H. Just, “Mathematical Tools for Spatial Computations with Biplane Isocentric X-Ray Equipment,” *Biomed. Tech.*, vol. 31, pp. 101–107, may 1986.

[18] A. Wahle, H. Oswald, G. A. Schulze, J. Beier, and E. Fleck, “{3-D} Reconstruction, Modelling and Viewing of Coronary Vessels,” in *Comput. Assist. Radiol. ({CAR} ’91)*, (Berlin, Heidelberg), pp. 669–676, Springer Berlin Heidelberg, 1991.

[19] A. Wahle, E. Wellnhofer, H. Oswald, and E. Fleck, “Biplane coronary angiography: accurate quantitative 3-D reconstruction without isocenter,” in *Proc. Comput. Cardiol. Conf.*, pp. 97–100, IEEE Comput. Soc. Press, 1993.

[20] A. Wahle, E. Wellnhofer, I. Mugaragu, H. U. Sauer, H. Oswald, and E. Fleck, “Assessment of Diffuse Coronary Artery Disease by Quantitative Analysis of Coronary Morphology Based upon 3-D Reconstruction from Biplane Angiograms,” *IEEE Trans. Med. Imaging*, vol. 14, pp. 230–241, jun 1995.

[21] Rosenfield *et al.*, “Three-dimensional reconstruction of human coronary and peripheral arteries from images recorded during two-dimensional intravascular ultrasound examination,” *Circulation*, vol. 84, pp. 1938–1956, nov 1991.

[22] J. Honye, D. J. Mahon, and J. M. Tobis, “Intravascular ultrasound imaging,” *Trends Cardiovasc. Med.*, vol. 1, pp. 305–311, oct 1991.

[23] Roelandt *et al.*, “Three-dimensional reconstruction of intracoronary ultrasound images: Rationale, approaches, problems, and directions,” *Circulation*, vol. 90, pp. 1044–1055, aug 1994.

[24] Bruining *et al.*, “Dynamic three-dimensional reconstruction of ICUS images based on an ecg-gated pull-back device,” *Proc. Comput. Cardiol.*, pp. 633–636, 1995.

[25] a. o. Laban, "ANGUS: A new approach to three-dimensional reconstruction of coronary vessels by combined use of angiography and intravascular ultrasound," in *Comput. Cardiol. 1995*, vol. 95, pp. 325–328, IEEE, 1995.

[26] R. Shekhar, R. Cothren, D. Vince, and J. Cornhill, "Fusion of intravascular ultrasound and biplane angiography for three-dimensional reconstruction of coronary arteries," in *Comput. Cardiol. 1996*, pp. 5–8, IEEE, 1996.

[27] Evans *et al.*, "Accurate three-dimensional reconstruction of intravascular ultrasound data. Spatially correct three-dimensional reconstructions.," *Circulation*, vol. 93, pp. 567–76, feb 1996.

[28] G. P. Prause, S. C. DeJong, C. R. McKay, and M. Sonka, "Towards a geometrically correct 3-D reconstruction of tortuous coronary arteries based on biplane angiography and intravascular ultrasound.," *Int. J. Card. Imaging*, vol. 13, pp. 451–462, dec 1997.

[29] K. R. Subramanian, M. J. Thubrikar, B. Fowler, M. T. Mostafavi, and M. W. Funk, "Accurate 3D reconstruction of complex blood vessel geometries from intravascular ultrasound images: in vitro study," *J. Med. Eng. Technol.*, vol. 24, no. 4, pp. 131–140, 2000.

[30] D. H. U. Kochanek, R. H. Bartels, D. H. U. Kochanek, and R. H. Bartels, "Interpolating splines with local tension, continuity, and bias control," in *Proc. 11th Annu. Conf. Comput. Graph. Interact. Tech. - SIGGRAPH '84*, vol. 18, (New York, New York, USA), pp. 33–41, ACM Press, 1984.

[31] Bourantas *et al.*, "A method for 3D reconstruction of coronary arteries using biplane angiography and intravascular ultrasound images," *Comput. Med. Imaging Graph.*, vol. 29, pp. 597–606, dec 2005.

[32] S. Zheng, "Three-dimensional reconstruction of vessels from intravascular ultrasound sequence and X-ray angiograms," in *Proc. 2009 2nd Int. Conf. Biomed. Eng. Informatics, BMEI 2009*, pp. 1–5, IEEE, 2009.

[33] Carlier *et al.*, "A new method for real-time co-registration of 3D coronary angiography and intravascular ultrasound or optical coherence tomography," jun 2014.

[34] J. W. Goodman, *Speckle Phenomena in Optics: Theory and Applications*. Englewood, Colorado.: Robert and Compant, 2007.

[35] K. Iizuka, *Elements of Photonics, Volume II*, vol. 2. Wiley-Interscience, 2002.

[36] K. T. Grattan and T. Sun, "Fiber optic sensor technology: An overview," *Sensors Actuators, A Phys.*, vol. 82, pp. 40–61, may 2000.

[37] B. Lee, "Review of the present status of optical fiber sensors," *Opt. Fiber Technol.*, vol. 9, no. 2, pp. 57–79, 2003.

[38] G. Allwood, G. Wild, and S. Hinckley, "Fiber bragg grating sensors for mainstream industrial processes," oct 2017.

[39] C. Truesdell, W. Noll, and S. S. Antman, *The non-linear field theories of mechanics, Volume 3.* Springer, 2004.

[40] K. R. Henken, J. Dankelman, J. J. Van Den Dobbelsteen, L. K. Cheng, and M. S. Van Der Heiden, "Error analysis of FBG-based shape sensors for medical needle tracking," *IEEE/ASME Trans. Mechatronics*, vol. 19, pp. 1523–1531, oct 2014.

[41] D. A. Krohn, T. MacDougall, and A. Mendez, *Fiber optic sensors: Fundamentals and applications: Fourth edition*, vol. 4th. Society of Photo-Optical Instrumentation Engineers (SPIE), 2015.

[42] K. Henken, D. Van Gerwen, J. Dankelman, and J. Van Den Dobbelsteen, "Accuracy of needle position measurements using fiber Bragg gratings," *Minim. Invasive Ther. Allied Technol.*, vol. 21, pp. 408–414, nov 2012.

[43] M. S. van der Heiden, K. R. Henken, L. K. Cheng, B. G. van den Bosch, R. van den Braber, J. Dankelman, and J. J. van den Dobbelsteen, "Accurate and efficient fiber optical shape sensor for MRI compatible minimally invasive instruments," *Opt. Syst. Des. 2012*, vol. 8550, pp. 1–14, dec 2012.

[44] X. Yi, J. Qian, L. Shen, Y. Zhang, and Z. Zhang, "An innovative 3D colonoscope shape sensing sensor based on FBG sensor array," in *Proc. 2007 Int. Conf. Inf. Acquis. ICIA*, pp. 227–232, IEEE, jul 2007.

[45] Y. L. Park, S. Elayaperumal, B. Daniel, S. C. Ryu, M. Shin, J. Savall, R. J. Black, B. Moslehi, and M. R. Cutkosky, "Real-time estimation of 3-D needle shape and deflection for MRI-guided interventions," *IEEE/ASME Trans. Mechatronics*, vol. 15, pp. 906–915, dec 2010.

[46] C. E. Campanella, A. Cuccovillo, C. Campanella, A. Yurt, and V. M. Passaro, "Fibre Bragg Grating based strain sensors: Review of technology and applications," sep 2018.

[47] V. Varyshchuk and Y. Bobitski, "Correlation processing of speckle pattern in multimode polymer optical fiber for deformation monitoring in nanometer range," in *Springer Proceedings in Physics*, vol. 167, pp. 329–338, Springer Science and Business Media, LLC, 2015.

[48] W. B. Spillman, B. R. Kline, L. B. Maurice, and P. L. Fuhr, "Statistical-mode sensor for fiber optic vibration sensing uses," *Applied Optics*, vol. 28, p. 3166, aug 1989.

[49] K. Pan, C. M. Uang, F. Cheng, and F. T. Yu, "Multimode fiber sensing by using mean-absolute speckle-intensity variation.," *Applied optics*, vol. 33, pp. 2095–8, apr 1994.

[50] J. A. Leendertz, "Interferometric displacement measurement on scattering surfaces utilizing speckle effect," *Journal of Physics E: Scientific Instruments*, vol. 3, pp. 214–218, mar 1970.

[51] F. T. S. Yu, J. Zhang, K. Pan, D. Zhao, and P. B. Ruffin, "Fiber vibration sensor that uses the speckle contrast ratio," *Optical Engineering*, vol. 34, pp. 236–239, jan 1995.

[52] E. Fujiwara, Y. T. Wu, and C. K. Suzuki, "Vibration-based specklegram fiber sensor for measurement of properties of liquids," *Optics and Lasers in Engineering*, vol. 50, pp. 1726–1730, dec 2012.

[53] A. Garcia-Valenzuela and M. Tabib-Azar, "Fiber-optic force and displacement sensor based on speckle detection with 0.1 nN and 0.1 Å resolution," *Sensors and Actuators: A. Physical*, vol. 36, pp. 199–208, may 1993.

[54] E. Fujiwara, F. Paula, Y. Wu, M. Santos, and C. Suzuki, "Optical fiber tactile sensor for user interfaces," *Proc. Int. Symp. Consum. Electron. ISCE*, vol. 2, pp. 8–9, sep 2016.

[55] F. T. Yu, M. Wen, S. Yin, and C. M. Uang, "Submicrometer displacement sensing using inner-product multimode fiber speckle fields.," *Applied optics*, vol. 32, pp. 4685–9, sep 1993.

[56] S. Qian, Y. Xu, L. Zhong, and L. Su, "Investigation on sensitivity enhancement for optical fiber speckle sensors," *Optics Express*, vol. 24, p. 10829, may 2016.

[57] L. Di Stefano, S. Mattoccia, and F. Tombari, "ZNCC-based template matching using bounded partial correlation," *Pattern Recognit. Lett.*, vol. 26, pp. 2129–2134, oct 2005.

[58] B. Srinivasa Reddy and B. N. Chatterji, "An FFT-based technique for translation, rotation, and scale-invariant image registration," *IEEE Trans. Image Process.*, vol. 5, no. 8, pp. 1266–1271, 1996.

[59] J. B. Maintz and M. A. Viergever, "A survey of medical image registration," *Med. Image Anal.*, vol. 2, no. 1, pp. 1–36, 1998.

[60] E. Fujiwara, Y. Ri, Y. T. Wu, H. Fujimoto, and C. K. Suzuki, "Evaluation of image matching techniques for optical fiber specklegram sensor analysis," *Appl. Opt.*, vol. 57, no. 33, p. 9845, 2018.

[61] E. Fujiwara, L. E. da Silva, T. D. Cabral, H. E. de Freitas, Y. T. Wu, and C. M. d. B. Cordeiro, "Optical Fiber Specklegram Chemical Sensor Based on a Concatenated Multimode Fiber Structure," *J. Light. Technol.*, vol. 37, pp. 5041–5047, jul 2019.

[62] Eric Fujiwara, M. F. M. dos Santos, and C. K. Suzuki, "Optical fiber specklegram sensor analysis by speckle pattern division," *Applied Optics*, vol. 56, pp. 1585–1590, feb 2017.

[63] H. S. Efendioglu, T. Yildirim, O. Toker, and K. Fidanboylu, "Design of intelligent fiber optic statistical mode sensors using novel features and artificial neural networks," jul 2012.

[64] H. S. Efendioglu, "A Review of Fiber-Optic Modal Modulated Sensors: Specklegram and Modal Power Distribution Sensing," *IEEE Sens. J.*, vol. 17, no. 7, pp. 2055–2064, 2017.

[65] J. H. Merritt, M. Sayeh, and M. T. Mostafavi, "Intelligent Shape Sensor," in *ASPE Proceeding*, (Dallas, TX), 2007.

[66] E. Fujiwara, Y. T. Wu, M. F. M. dos Santos, E. A. Schenkel, and C. K. Suzuki, "Development of a tactile sensor based on optical fiber specklegram analysis and sensor data fusion technique," *Sensors and Actuators, A: Physical*, vol. 263, pp. 677–686, 2017.

[67] M. R. Sayeh, R. Viswanathan, and S. K. Dhali, "Neural networks for smart structures with fiber optic sensors," in *Applications of Optical Engineering: Proceedings of OE/Midwest '90*, vol. 1396, pp. 417–429, SPIE, mar 1991.

[68] M. Taib and R. Narayanaswamy, "Multichannel calibration technique for optical-fibre chemical sensor using artificial neural network," *Sensors and Actuators B: Chemical*, vol. 39, pp. 365–370, mar 1997.

[69] S. E. W. Chandrashekhara, G. W. Sanders, F. Akhavan, and K, "Modal analysis using fiber optic sensors and neural networks for prediction of composite beam delamination," *Smart Materials and Structures*, vol. 11, no. 4, p. 489, 2002.

[70] M. Aktas, T. Akgun, M. U. Demircin, and D. Buyukaydin, "Deep learning based multi-threat classification for phase-OTDR fiber optic distributed acoustic sensing applications," in *Fiber Optic Sensors and Applications XIV*, vol. 10208, p. 102080G, SPIE, apr 2017.

[71] A. R. Cuevas, M. Fontana, L. Rodriguez-Cobo, M. Lomer, and J. M. Lopez-Higuera, "Machine Learning for Turning Optical Fiber Specklegram Sensor into a Spatially-Resolved Sensing System. Proof of Concept," *Journal of Lightwave Technology*, vol. 36, pp. 3733–3738, sep 2018.

[72] B. A. Jones and I. D. Walker, "Kinematics for multisection continuum robots," *IEEE Trans. Robot.*, vol. 22, no. 1, pp. 43–55, 2006.

[73] H. Hu, P. Wang, B. Zhao, M. Li, and L. Sun, "Design of a novel snake-like robotic colonoscope," in *2009 IEEE Int. Conf. Robot. Biomimetics, ROBIO 2009*, pp. 1957–1961, 2009.

[74] I. D. Walker, "Continuous Backbone "Continuum" Robot Manipulators," *ISRN Robot.*, vol. 2013, pp. 1–19, 2013.

[75] S. Wang, J. Housden, D. Singh, K. Althoefer, and K. Rhode, "Design, testing and modelling of a novel robotic system for trans-oesophageal ultrasound," *Int. J. Med. Robot. Comput. Assist. Surg.*, vol. 12, pp. 342–354, sep 2016.

[76] E. J. Keogh and M. J. Pazzani, *Derivative Dynamic Time Warping*, pp. 1–11. Society for Industrial & Applied Mathematics (SIAM), apr 2001.

[77] E. L. E. L. Lehmann, *Nonparametrics : statistical methods based on ranks.* Holden-Day series in probability and statistics, San Francisco: Holden-Day, 1975.

[78] D.-H. Wang and P.-G. Jia, "Fiber optic extrinsic Fabry-Perot accelerometer using laser emission frequency modulated phase generated carrier demodulation scheme," *Opt. Eng.*, vol. 52, no. 5, p. 055004, 2013.

[79] S. Razmyar and T. Mostafavi, "A novel multi-mode fiber optic accelerometer: an intelligent sensor," in *Fiber Opt. Sensors Appl. XV*, vol. 10654, p. 17, SPIE, 2018.

[80] M. D. Zeiler and R. Fergus, "Visualizing and understanding convolutional networks," in *Lect. Notes Comput. Sci. (including Subser. Lect. Notes Artif. Intell. Lect. Notes Bioinformatics)*, vol. 8689 LNCS, pp. 818–833, Springer Verlag, 2014.

[81] R. R. Selvaraju, M. Cogswell, A. Das, R. Vedantam, D. Parikh, and D. Batra, "Grad-CAM: Visual Explanations from Deep Networks via Gradient-Based Localization," in *Proc. IEEE Int. Conf. Comput. Vis.*, vol. 2017-Octob, pp. 618–626, Institute of Electrical and Electronics Engineers Inc., dec 2017.

[82] D. P. Kingma and J. L. Ba, "Adam: A method for stochastic optimization," in *3rd Int. Conf. Learn. Represent. ICLR 2015 - Conf. Track Proc.*, International Conference on Learning Representations, ICLR, 2015.

[83] R. A. Serway, J. W. Jewett, and V. Peroomian, *Physics for scientists and engineers with modern physics.* MA Cengage, 2019.

[84] J. Kalenik and R. PajaÌ§k, "A cantilever optical-fiber accelerometer," *Sensors and Actuators, A: Physical*, vol. 68, pp. 350–355, jun 1998.

[85] B. S. Miller, T. Soares, Y. V. Weddingen, and J. Wendlandt, "Modeling Flexible Bodies with Simscape Multibody Software." `https://www.mathworks.com/campaigns/offers/model-flexible-bodies.htm`. Accessed: 2019-09-30.

[86] D. Li, L. Ren, and H. Li, "Mechanical Property and Strain Transferring Mechanism in Optical Fiber Sensors," in *Fiber Optic Sensors*, InTech, feb 2012.

[87] Y. P. Xiong, J. T. Xing, and W. G. Price, "A general linear mathematical model of power flow analysis and control for integrated structure-control systems," *Journal of Sound and Vibration*, vol. 267, pp. 301–334, oct 2003.

[88] S. Hochreiter and J. Urgen Schmidhuber, “Long Short-term Memory,” *Neural Comput.*, vol. 9, no. 8, pp. 1735–1780, 1997.

[89] R. Parent, D. S. Ebert, D. Gould, M. Gross, C. Kazmier, C. J. Lumsden, R. Keiser, A. Menache, M. Müller, F. K. Musgrave, M. V. Pauly, D. Peachey, K. Perlin, H. Pfister, J. Sharpe, M. R. Wilkins, M. Wicke, N. Woolridge, and S. Worley, *Computer Animation Complete: All-in-One: Learn Motion Capture, Characteristic, Point-Based, and Maya Winning Techniques*. Elsevier, 2009.